Acta Mechanica

Volume 233, issue 4, April 2022

24 articles in this issue

Physical models and vortex dynamics of swimming and flying: a review

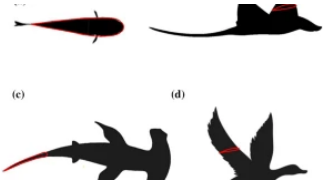

Dong Zhang, Jun-Duo Zhang & Wei-Xi Huang

Review and Perspective in Mechanics (by invitation only)

Published: 12 April 2022 | Pages: 1249 - 1288

Intense cross-scale energy cascades resembling “mechanical turbulence” in harmonically driven strongly nonlinear hierarchical chains of oscillators

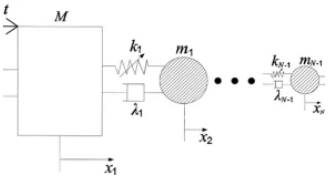

Jian En Chen, Timo Theurich ... Alexander F. Vakakis

Original Paper | Published: 13 March 2022

Pages: 1289 - 1305

The general basis-free spin and its concise proof

Chun-Yu Meng & Ming-Xiang Chen

Original Paper | Published: 17 March 2022 | Pages: 1307 - 1316

A directional-dependent localized mass-field damage model for anisotropic brittle fracture

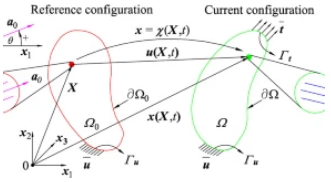

Hung Thanh Tran & Tinh Quoc Bui

Original Paper | Published: 16 February 2022 |

Pages: 1317 - 1336

Correction to: A directional-dependent localized mass-field damage model for anisotropic brittle fracture

Hung Thanh Tran & Tinh Quoc Bui

Correction | Published: 01 April 2022 | Pages: 1337 - 1337

Non-stationary heat transfer in composite membrane with circular inclusions in hexagonal lattice structures

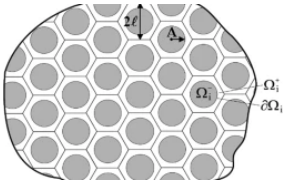

I. V. Andrianov, J. Awrejcewicz & G. A. Starushenko

Original Paper | Published: 19 March 2022 |

Pages: 1339 - 1350

Probabilistic thermal stability of laminated composite plates with temperature-dependent properties under a stochastic thermal field

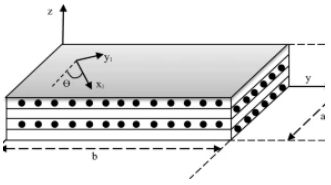

Hadi Parviz, Mahdi Fakoor & Fatemeh Hosseini

Original Paper | Published: 19 March 2022 |

Pages: 1351 - 1370

A copula-function-based structural system reliability analysis method

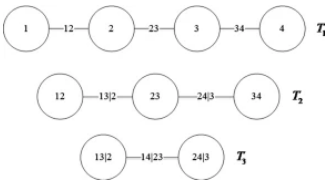

D. Mi, W. Zhang ... C. Jiang

Original Paper | Published: 22 March 2022

Pages: 1371 - 1391

Nonlinear planar vibrations of a cable with a linear damper

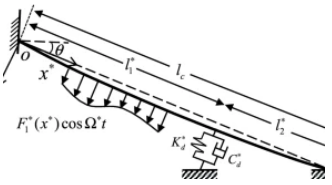

Xiaoyang Su, Houjun Kang ... Weidong Zhu

Original Paper | Published: 24 March 2022

Pages: 1393 - 1412

The effect of voids shape on hypervelocity cylindrical cavity expansion and shock waves formation in transversely isotropic porous materials

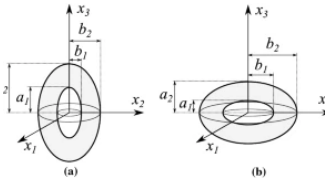

T. dos Santos, J. C. Nieto-Fuentes ... J. A. Rodríguez-Martínez

Original Paper | Published: 25 March 2022

Pages: 1413 - 1434

Frictional moving contact problem between a functionally graded monoclinic layer and a rigid punch of an arbitrary profile

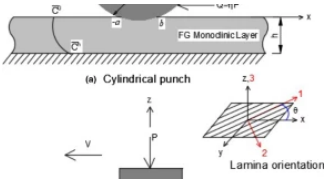

İsa Çömez

Original Paper | Published: 26 March 2022

Pages: 1435 - 1453

Dynamic stress concentration of a non-circular cavern in a viscoelastic medium subjected to a plane P-wave

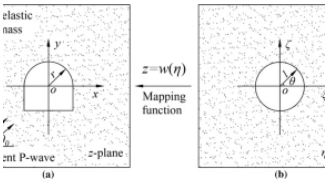

X. Wang & X. P. Zhang

Original Paper | Published: 30 March 2022

Pages: 1455 - 1466

The meshless local Petrov–Galerkin cumulant lattice Boltzmann method: strengths and weaknesses in aeroacoustic analysis

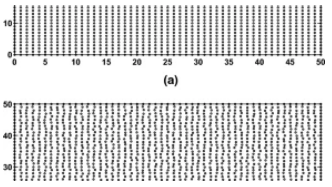

Mohsen Gorakifard, Clara Salueña ... Ehsan Kian Far

Original Paper | Published: 06 April 2022

Pages: 1467 - 1483

On the dynamic stability of delaminated composite beams under free vibration

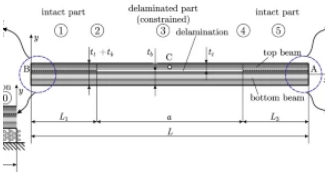

András Szekrényes, Péter Máté & Bence Hauck

Original Paper | Open Access | Published: 07 April 2022

Pages: 1485 - 1512

On the mechanics of strain localization in plasticity: isotropic and orthotropic, elasto- and rigid-plastic, associated and non-associated models

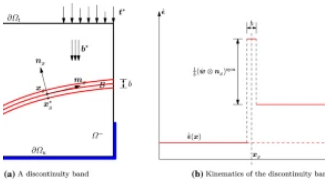

Miguel Cervera, Jian-Ying Wu ... Michele Chiumenti

Original Paper | Published: 07 April 2022

Pages: 1513 - 1542

Delay or control of flow separation for enhanced aerodynamic performance using an effective morphed surface

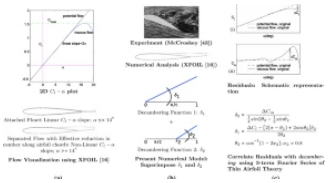

Aritras Roy & Rinku Mukherjee

Original Paper | Published: 09 April 2022

Pages: 1543 - 1566

Free vibration analysis of combined composite laminated conical–cylindrical shells with varying thickness using the Haar wavelet method

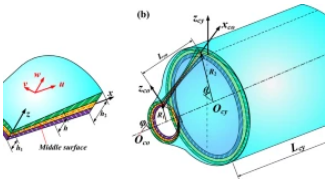

Kwanghun Kim, Songhun Kwak ... Kwangil Choe

Original Paper | Published: 09 April 2022

Pages: 1567 - 1597

Nonlinear bending of FG skew sandwich plates with temperature-dependent elastoplastic properties using an enhanced 3D meshless approach

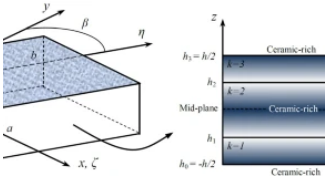

Reza Vaghefi

Original Paper | Published: 10 April 2022

Pages: 1599 - 1631

Nonlinear random vibration of functionally graded nanobeams based on the nonlocal strain gradient theory

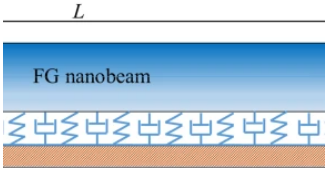

N. D. Anh & D. V. Hieu

Original Paper | Published: 10 April 2022

Pages: 1633 - 1648

The scattering of SH-waves by a nano arc-shaped hole on a half-plane

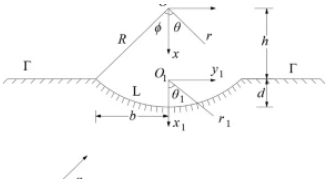

Hongmei Wu & Zhiying Ou

Original Paper | Published: 11 April 2022

Pages: 1649 - 1662

Energy flow and performance of a nonlinear vibration isolator exploiting geometric nonlinearity by embedding springs in linkages

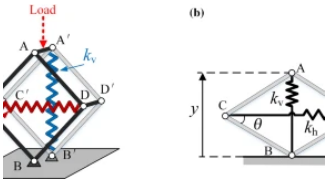

Wei Dai, Tianyun Li & Jian Yang

Original Paper | Published: 12 April 2022 |

Pages: 1663 - 1687

Displacement-based and stress-based analytical approaches for nonlinear bending analysis of functionally graded porous plates resting on elastic substrate

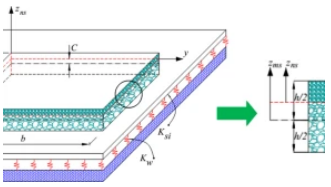

Nguyen Van Long, Tran Minh Tu ... Vu Thi Thu Trang

Original Paper | Published: 15 April 2022 |

Pages: 1689 - 1714

Correction to: A mode-matching method for the prediction of stick-slip relative motion of two elastic rods in frictional contact

Athanasios Tsetas, Apostolos Tsouvalas ... Andrei V. Metrikine

Correction | Open Access | Published: 17 March 2022 | Pages: 1715 - 1715

Correction to: Study of the SH-wave propagation in an FGPM layer imperfectly bonded over a microstructural coupled stress half-space

Bhanu Pratap Rajak, Santimoy Kundu & Shishir Gupta

Correction | Published: 18 March 2022 | Pages: 1717 - 1717

For authors

Submission guidelines
Ethics & disclosures

Open Access fees and funding

Open Access fees and funding

Contact the journal

Submit manuscript

Explore

Online first articles

Volumes and issues

Sign up for alerts

Acta Mech
https://doi.org/10.1007/s00707-022-03196-5

ORIGINAL PAPER

Nguyen Van Long · Tran Minh Tu · Huong Quy Truong · Le Thanh Hai · Vu Thi Thu Trang

Displacement-based and stress-based analytical approaches for nonlinear bending analysis of functionally graded porous plates resting on elastic substrate

Received: 20 October 2021 / Revised: 23 January 2022 / Accepted: 10 March 2022

Abstract For the first time, displacement-based and stress-based approaches are used simultaneously to analyze the nonlinear bending response of functionally graded porous plates within the framework of first-order shear deformation theory. Three configurations of porosity distributions including uniform, nonuniform symmetric, and nonuniform asymmetric are selected. Utilizing the Galerkin method, the neutral surface position concept, and the solutions in terms of Fourier series, the nonlinear algebraic governing equations are derived and then solved by the Newton–Raphson method. Very good agreement is found in the comparison between results obtained by using two proposed approaches, and in comparisons with those of existing ones in the literature. Parametric studies are conducted to evaluate the influence of the porosity coefficient, porosity distribution configurations, geometrical parameters, Pasternak elastic foundation, and boundary conditions on the load–deflection and load-bending moment curves.

1 Introduction

One of the most important inventions in advanced materials was the introduction of functionally graded materials (FGMs) by Japanese scientists in the 1980s. On the macroscopic scale, FGMs are anisotropic, inhomogeneous, usually made up of two constituents, metal and ceramic, in which the mechanical properties of the material change smoothly and continuously from one surface to the other. Recently, a new generation of FGM called functionally graded porous materials (FGPMs) with pores in the microstructure is known as a lightweight material, in which the porosity distribution patterns and porosity coefficient are design variables, which can be adjusted to achieve the desired mechanical properties. Light structures using FGPMs such as metal foam have potential applications in aviation, marine, biomedical, civil construction, and transportation industries [1–3]. With a high stiffness-to-weight ratio, excellent energy absorption, very good acoustic, and thermal isolation, metal foam is a suitable choice for making insulating acoustical, thermal panels, components that enable withstand dynamic loads or impact loads. Along with the increase in application, research on the mechanical behavior of structures using FGPMs has attracted the attention of the scientific community. Most of these studies focus on the linear analysis of bending, vibration, and stability behavior of FGM beam, plate, and shell structures [4–10]. Mechanical/structural components may undergo large deflection such as morphing aerostructures, soft robotic arms, highly flexible and lightweight aircraft wings, and wind turbine blades [11].

N. V. Long · T. M. Tu (✉) · H. Q. Truong
Faculty of Industrial and Civil Engineering, Hanoi University of Civil Engineering, Hanoi, Vietnam
e-mail: tutm@nuce.edu.vn

L. T. Hai
Faculty of Civil Engineering, Vinh University, Vinh, Vietnam

V. T. T. Trang
School of Mechanical Engineering, Vietnam Maritime University, Haiphong, Vietnam

Published online: 15 April 2022

To describe more closely the actual behavior of the structure, nonlinear analyses are often used with consideration of the geometric nonlinearity in strains. There are numerous studies focusing on the nonlinear bending response of FG plates using the numerical approach. By employing first-order shear deformation theory (FSDT) including geometrical nonlinearity, Praveen và Reddy [12] presented the nonlinear transient analysis of FG plates under thermomechanical loading by finite element method (FEM). Aliaga and Reddy [13] performed the nonlinear static and transient analysis of the FGM plate imposed in a high-temperature environment using FEM. Zhao và Liew [14] predicted the nonlinear displacements, and stresses of FG plates by using FSDT with geometrical nonlinearity and the mesh-free method. Using the Marguerre shell element, Barbosa and Ferreira [15] presented the nonlinear response of FG flat and curved panels. By using FEM, Behjat and Khoshravan [16] presented nonlinear bending and vibrational characteristic of FG piezoelectric plates under mechanical loads including piezoelectric effect. Singh and Shukla [17] utilized the multiquadric radial basis function method and quadratic extrapolation technique to explore the nonlinear flexural response of FG plates. Zhu et al. [18] implemented the local Kriging meshless method to study the thermal effect on the nonlinear behavior of FG plates. Employing isogeometric analysis (IA) in conjunction with FSDT taking into account geometrical nonlinearity, Yin et al. [19] investigated influences of FGM parameters, geometrical shape on nonlinear transverse displacement and axial stresses of FG plates. Heydari et al. [20] investigated the effect of CNT distribution configurations on the large deflection analysis of FG-CNTR plates. Employing smoothed FEM, Phung-Van et al. [21] probed the nonlinear response of FG plates under mechanical and thermal loads. Using the meshless method with radial point interpolation, Nourmohammadi and Behjat [22] explored the nonlinear response of FG piezoelectric plates. Based on FSDT taking into account nonlinear strains, Ton-That et al. [23] adopted a four-node quadrilateral element to explore the load–deflection curves of FG plates having different shapes and constraints.

Apart from the numerical methods mentioned in the above short review, semi-analytical and analytical methods are also effective tools often chosen by many authors for the nonlinear analysis of FG plates. Two approaches commonly used in published reports include the stress-based approach and the displacement-based approach.

Introducing stress function within the context of Reddy's HSDT including von Kárman nonlinearity, Shen [24] used a mixed Galerkin-perturbation technique to study the influence of temperature change on the nonlinear behavior of FG plate. Yang and Shen [25] used a semi-numerical method to analyze the nonlinear response of FG plate under uniform pressure including the thermal effect. Shen ad Wang [26] employed the perturbation method to determine the nonlinear flexural characteristic of FGM plates working in a thermal environment. Using thin plate theory including geometrical nonlinearity and initial imperfection, Tung và Duc [27] studied buckling and post-buckling of simply supported FG plates. Thang et al. [28] proposed an analytical approach to study post-buckling analysis of variable thickness sigmoid FG plates by using the thin plate theory in combination with stress function and the Galerkin method. Using TSDT and stress function, Duc et al. [29] analyzed the nonlinear dynamic behavior of thick FG plates. Based on classical plate theory with large transverse deflections, Woo et al. [30] studied nonlinear vibrational characteristics of FGM panels taking into account the thermal effect.

Using a displacement-based approach, several works associated with the nonlinear behavior of FG panels have been conducted. Employing double Chebyshev polynomial, Wu et al. [31] studied buckling and post-buckling responses of functionally graded plates under thermomechanical loading. Using minimum total potential energy principle and classical plate theory, Alinia and Ghannadpour [32] presented an analytical solution in the harmonic function form for geometrically nonlinear bending of functionally graded plates. Woo et al. [33] indicated the thermomechanical effect on the nonlinear flexural response of functionally graded plates and shells by using a series of displacement solutions. Using the energy method within the context of FSDT and HSDT, Khabbaz et al. [34] predicted the influence of geometrical parameters on the nonlinear deflection and stress components of FG plates. Herein, the displacement field is assumed as double trigonometric series satisfying simply supported boundary conditions. Benatta et al. [35] suggested a novel plate theory to analyze the nonlinear flexural behavior of FG plates by using the principle of minimum potential energy and double trigonometric series displacement solutions.

Recently, along with the introduction of FGP materials, nonlinear analyses of the mechanical behavior of FGP plates are increasingly interested; however, the published results in this field are still relatively limited. Some recent publications can be found in the reports of Duc et al. [36], Tu et al. [37], Cong et al. [38], Phung-Van et al. [39], Nguyen et al. [40], Ansari et al. [41], Nematollahi et al. [42], Selvamani et al. [43], etc.

In this paper, for the first time, both the stress-based approach and the displacement-based approach will be used simultaneously to analyze the nonlinear flexural response of an FGP plate interacting with an elastic

substrate under different boundary conditions. By using the concept of a physical neutral surface [44, 45], the stretching–bending couplings in constitutive equations are eliminated, and the governing equations become a simpler form, resulting in reduce computational time. It is especially effective for nonlinear problems. After verifying the accuracy of proposed approaches, the effect of porosity coefficient, porosity distribution configurations of FGPMs, plate geometric parameters, elastic foundation stiffness, and boundary conditions on load–deflection curves and load-moment curves are investigated.

2 Functionally graded porous plate

Considering a rectangular FGP plate of thickness h, dimensions in x, y—axes are length a and width b, respectively, as shown in Fig. 1. The coordinates of a point along the thickness direction can be represented in two coordinate systems, z_{ms} measured from the middle surface and z_{ns} from the neutral surface of the plate. The FGP plate resting on Pasternak's elastic foundation with K_w and K_{si} $(i = x, y)$ is the transverse and shear stiffness coefficients, respectively.

The open-cell porous material with three porosity distribution patterns (Fig. 2) is considered in this study. Elastic moduli of materials are defined as follows [4, 46–48]:

- Uniform porosity distribution (Type 1):

$$\{E, G\} = \left\{E_1^*, G_1^*\right\}(1 - e_0\chi);\ \chi = \frac{1}{e_0} - \frac{1}{e_0}\left(\frac{2}{\pi}\sqrt{1 - e_0} - \frac{2}{\pi} + 1\right)^2 \tag{1}$$

- Non-uniform symmetric porosity distribution (Type 2):

$$\{E(z_{ms}), G(z_{ms})\} = \left\{E_1^*, G_1^*\right\}[1 - e_0\cos(\pi z_{ms}/h)] \tag{2}$$

- Non-uniform asymmetric porosity distribution (Type 3):

$$\{E(z_{ms}), G(z_{ms})\} = \left\{E_1^*, G_1^*\right\}\left[1 - e_0\cos\frac{1}{2}(\pi z_{ms}/h + \pi/2)\right] \tag{3}$$

The porosity coefficients e_0 are given by:

$$e_0 = 1 - \frac{E_2^*}{E_1^*} = 1 - \frac{G_2^*}{G_1^*},\quad 0 < e_0 < 1, \tag{4}$$

in which E_1^*, G_1^* are the maximum values of Young's modulus and shear modulus, and E_2^*, G_2^* are minimum values, respectively. The extremum values of the Young's moduli are related to the extremum values of the shear moduli by $G_i^* = E_i^*/[2(1 + \nu)]$. Assume that Poisson's ratio ν is constant along with the plate thickness.

For the FGP plate with asymmetric distribution pattern, the neutral surface location has not coincided with the middle surface and is indicated from the condition [49]:

$$\int_{-h/2}^{h/2}(z_{ms} - C)E(z_{ms})\mathrm{d}z_{ms} = 0,\ \text{leading to;}\ C = \left[\int_{-h/2}^{h/2} z_{ms}E(z_{ms})dz\right] / \left[\int_{-h/2}^{h/2} E(z_{ms})\mathrm{d}z\right] \tag{5}$$

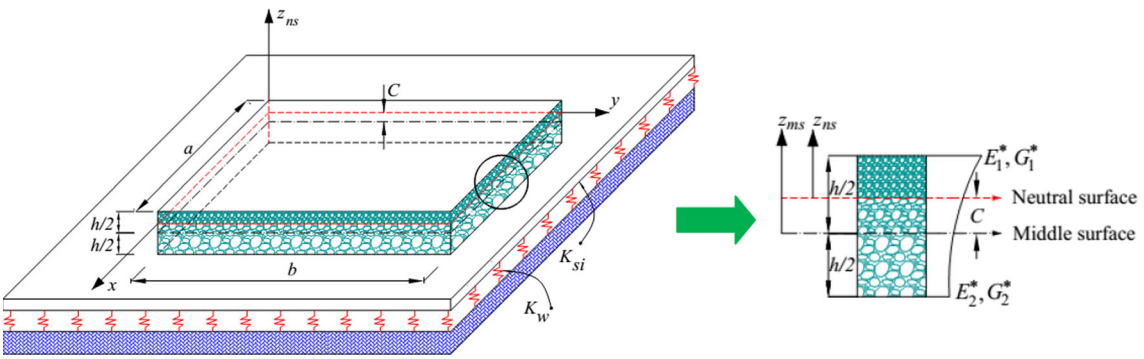

Fig. 1 The geometry and cross-section rectangular FGP plate resting on an elastic foundation

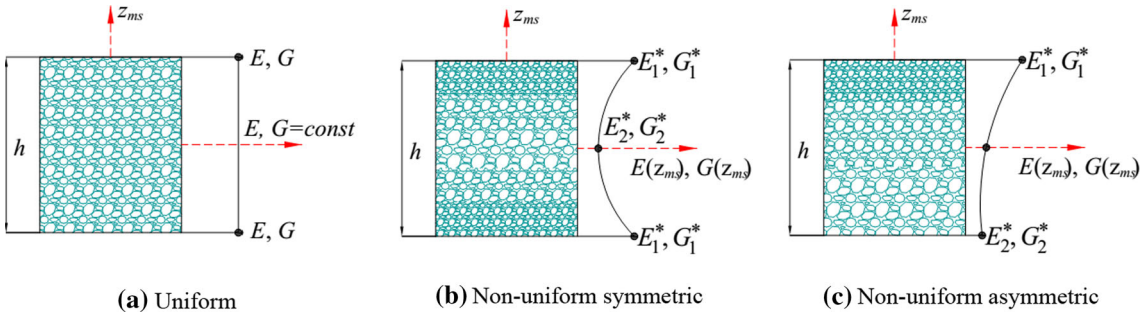

(a) Uniform **(b)** Non-uniform symmetric **(c)** Non-uniform asymmetric

Fig. 2 The FGP plate with different porosity distribution patterns

3 First-order shear deformation theory considering neutral surface position concept

Considering the neutral surface position concept, displacement components according to the FSDT are defined as below [50]:

$$\begin{aligned} u(x,\ y,\ z_{ns}) &= \overline{u}_0(x,\ y) + z_{ns}\overline{\theta}_x(x,\ y), \\ v(x,\ y,\ z_{ns}) &= \overline{v}_0(x,\ y) + z_{ns}\overline{\theta}_y(x,\ y), \\ w(x,\ y,\ z_{ns}) &= \overline{w}_0(x,\ y), \end{aligned} \tag{6}$$

where $\overline{u}_0$, $\overline{v}_0$ and $\overline{w}_0$ are displacements of the mid-plane in the x, y, and z directions, and $\overline{\theta}_x$ and $\overline{\theta}_y$ are rotations of the normals about the y and x-axes, respectively.

Nonzero strains including von Kármán geometric nonlinearity are defined as [50]:

$$\left\{\begin{array}{c}\varepsilon_x\\ \varepsilon_y\\ \gamma_{xy}\end{array}\right\} = \left\{\begin{array}{c}\varepsilon_x^0\\ \varepsilon_y^0\\ \gamma_{xy}^0\end{array}\right\} + z_{ns}\left\{\begin{array}{c}\kappa_x\\ \kappa_y\\ \kappa_{xy}\end{array}\right\},\ \left\{\begin{array}{c}\gamma_{xz}\\ \gamma_{yz}\end{array}\right\} = \left\{\begin{array}{c}\gamma_{xz}^0\\ \gamma_{yz}^0\end{array}\right\}, \tag{7}$$

in which $\varepsilon_x^0 = \overline{u}_{0,x} + \frac{1}{2}\overline{w}_{0,x}^2,\ \varepsilon_y^0 = \overline{v}_{0,y} + \frac{1}{2}\overline{w}_{0,y}^2,\ \gamma_{xy}^0 = \overline{u}_{0,y} + \overline{v}_{0,x} + \overline{w}_{0,x}\overline{w}_{0,y},$

$$k_x = \overline{\theta}_{x,x},\ k_y = \overline{\theta}_{y,y},\ k_{xy} = \overline{\theta}_{x,y} + \overline{\theta}_{y,x},\ \gamma_{xz}^0 = \overline{w}_{0,x} + \overline{\theta}_x,\ \ \gamma_{yz}^0 = \overline{w}_{0,y} + \overline{\theta}_y,$$

where the subscript commas denote the partial differentiation with respect to the spatial variables.

From Hooke's law, stress components are determined as:

$$\left\{\begin{array}{c}\overline{\sigma}_x\\ \overline{\sigma}_y\\ \overline{\sigma}_{xy}\end{array}\right\} = \left[\begin{array}{ccc}\tilde{Q}_{11} & \tilde{Q}_{12} & 0\\ \tilde{Q}_{21} & \tilde{Q}_{22} & 0\\ 0 & 0 & \tilde{Q}_{66}\end{array}\right]\left\{\begin{array}{c}\varepsilon_x\\ \varepsilon_y\\ \gamma_{xy}\end{array}\right\},\ \left\{\begin{array}{c}\overline{\sigma}_{xz}\\ \overline{\sigma}_{yz}\end{array}\right\} = \left[\begin{array}{cc}\tilde{Q}_{55} & 0\\ 0 & \tilde{Q}_{44}\end{array}\right]\left\{\begin{array}{c}\gamma_{xz}\\ \gamma_{yz}\end{array}\right\}, \tag{8}$$

where $\tilde{Q}_{11} = \tilde{Q}_{22} = \frac{E(z_{ns})}{1-\nu^2}, \tilde{Q}_{12} = \tilde{Q}_{21} = \frac{\nu E(z_{ns})}{1-\nu^2}, \tilde{Q}_{44} = \tilde{Q}_{55} = \tilde{Q}_{66} = \frac{E(z_{ns})}{2(1+\nu)}$.

The stress resultants of a plate are obtained in the form:

$$\begin{aligned} &\left\{\begin{array}{c}N_x\\ N_y\\ N_{xy}\end{array}\right\} = \left[\begin{array}{ccc}\tilde{A}_{11} & \tilde{A}_{12} & 0\\ \tilde{A}_{12} & \tilde{A}_{11} & 0\\ 0 & 0 & \tilde{A}_{66}\end{array}\right]\left\{\begin{array}{c}\varepsilon_x^0\\ \varepsilon_y^0\\ \gamma_{xy}^0\end{array}\right\},\ \left\{\begin{array}{c}M_x\\ M_y\\ M_{xy}\end{array}\right\} = \left[\begin{array}{ccc}\tilde{C}_{11} & \tilde{C}_{12} & 0\\ \tilde{C}_{12} & \tilde{C}_{11} & 0\\ 0 & 0 & \tilde{C}_{66}\end{array}\right]\left\{\begin{array}{c}\kappa_x\\ \kappa_y\\ \kappa_{xy}\end{array}\right\}, \\ &\left\{\begin{array}{c}Q_{xz}\\ Q_{yz}\end{array}\right\} = \left[\begin{array}{cc}\tilde{A}_{44}^s & 0\\ 0 & \tilde{A}_{44}^s\end{array}\right]\left\{\begin{array}{c}\gamma_{xz}^0\\ \gamma_{yz}^0\end{array}\right\}, \end{aligned} \tag{9}$$

where $\left(\tilde{A}_{ij}, \tilde{C}_{ij}\right) = \int_{-h/2-C}^{h/2-C} \tilde{Q}_{ij}\left(1, \overline{z}_{ns}^2\right)\mathrm{d}\overline{z}_{ns};\ ij = 11,\ 12,\ 66$. The shear correction factor $k_s = 5/6$ is employed in this study.

The equilibrium equations are derived according to the minimum total potential energy principle [51]:

$$0 = \delta U_P + \delta U_F + \delta V, \tag{10}$$

in which δU_P, δU_F, and δV are variations of the strain energy, the potential energy of elastic foundation, and the potential energy of external load, respectively.

The obtained equilibrium equations can be expressed as below [51]:

$$N_{x,x} + N_{xy,y} = 0, \tag{11a}$$

$$N_{xy,x} + N_{y,y} = 0, \tag{11b}$$

$$Q_{xz,x} + Q_{yz,y} + N_x \overline{w}_{0,xx} + 2N_{xy}\overline{w}_{0,xy} + N_y \overline{w}_{0,yy} - K_w \overline{w}_0 + K_{sx}\overline{w}_{0,xx} + K_{sy}\overline{w}_{0,yy} + q = 0, \tag{11c}$$

$$M_{x,x} + M_{xy,y} - Q_{xz} = 0, \tag{11d}$$

$$M_{xy,x} + M_{y,y} - Q_{yz} = 0. \tag{11e}$$

From Eqs. (7), (9), and (11), the governing equations in terms of displacements can be written in the form:

$$\begin{aligned}&\tilde{A}_{11}\left(\overline{u}_{0,xx} + \overline{w}_{0,x}\overline{w}_{0,xx}\right) + \tilde{A}_{12}\left(\overline{v}_{0,xy} + \overline{w}_{0,y}\overline{w}_{0,xy}\right)\\ &\quad + \tilde{A}_{66}\left(\overline{u}_{0,yy} + \overline{v}_{0,xy} + \overline{w}_{0,x}\overline{w}_{0,yy} + \overline{w}_{0,y}\overline{w}_{0,xy}\right) = 0,\end{aligned} \tag{12a}$$

$$\begin{aligned}&\tilde{A}_{12}\left(\overline{u}_{0,xy} + \overline{w}_{0,x}w_{0,xy}\right) + \tilde{A}_{11}\left(\overline{v}_{0,yy} + \overline{w}_{0,y}\overline{w}_{0,yy}\right)\\ &\quad + \tilde{A}_{66}\left(\overline{u}_{0,xy} + \overline{v}_{0,xx} + \overline{w}_{0,xx}\overline{w}_{0,y} + \overline{w}_{0,x}\overline{w}_{0,xy}\right) = 0,\end{aligned} \tag{12b}$$

$$\begin{aligned}&\tilde{A}^s_{44}\overline{w}_{0,yy} + \tilde{A}^s_{44}\overline{w}_{0,xx} - K_w\overline{w}_0 + K_{sx}\overline{w}_{0,xx} + K_{sy}\overline{w}_{0,yy} + \tilde{A}^s_{44}\overline{\theta}_{x,x} + \tilde{A}^s_{44}\overline{\theta}_{y,y} + \tilde{A}_{11}\overline{u}_{0,x}\overline{w}_{0,xx}\\ &+\tilde{A}_{12}\overline{u}_{0,x}\overline{w}_{0,yy} + 2\tilde{A}_{66}\overline{u}_{0,y}\overline{w}_{0,xy} + \tilde{A}_{12}\overline{v}_{0,y}\overline{w}_{0,xx} + \tilde{A}_{11}\overline{v}_{0,y}\overline{w}_{0,yy} + 2\tilde{A}_{66}\overline{v}_{0,x}\overline{w}_{0,xy} + \frac{\tilde{A}_{11}}{2}\overline{w}^2_{0,x}\overline{w}_{0,xx}\\ &+\frac{\tilde{A}_{12}}{2}\overline{w}^2_{0,y}\overline{w}_{0,xx} + \frac{\tilde{A}_{12}}{2}\overline{w}^2_{0,x}\overline{w}_{0,yy} + \frac{\tilde{A}_{11}}{2}\overline{w}^2_{0,y}\overline{w}_{0,yy} + 2\tilde{A}_{66}\overline{w}_{0,x}\overline{w}_{0,y}\overline{w}_{0,xy} + q = 0,\end{aligned} \tag{12c}$$

$$\tilde{C}_{11}\theta_{x,xx} + \tilde{C}_{66}\theta_{x,yy} + \left(\tilde{C}_{12} + \tilde{C}_{66}\right)\overline{\theta}_{y,xy} - \tilde{A}^s_{44}\overline{\theta}_x - \tilde{A}^s_{55}\overline{w}_{0,x} = 0, \tag{12d}$$

$$\left(\tilde{C}_{12} + \tilde{C}_{66}\right)\overline{\theta}_{x,xy} + \tilde{C}_{66}\overline{\theta}_{y,xx} + \tilde{C}_{11}\overline{\theta}_{y,yy} - \tilde{A}^s_{44}\overline{\theta}_y - \tilde{A}^s_{44}\overline{w}_{0,y} = 0. \tag{12e}$$

4 Solution methodology

4.1 Displacement-based approach

Herein, three cases of boundary conditions (BCs) are considered as follows.

– **Case 1a** (SSSS-DB): All four edges of plates are simply supported and immovable. The associated BCs are:

$$\overline{u}_n = \overline{u}_s = \overline{w}_0 = \overline{\theta}_s = 0,\ M_n = 0 \tag{13}$$

– **Case 2a** (CCCC-DB): All four edges of the plates are clamped and immovable. The associated BCs are:

$$\overline{u}_n = \overline{u}_s = \overline{w}_0 = \overline{\theta}_n = \overline{\theta}_s = 0 \tag{14}$$

– **Case 3** (SCSC-DB): Two opposite edges are simply supported, and the others are clamped and immovable. The associated BCs are:

$$\begin{aligned}&\text{At } x = 0, a\text{: } \overline{u}_0 = \overline{v}_0 = \overline{w}_0 = \overline{\theta}_y = 0,\ M_x = 0\\ &\text{At } y = 0, b\text{: } \overline{u}_0 = \overline{v}_0 = \overline{w}_0 = \overline{\theta}_x = \overline{\theta}_y = 0\end{aligned} \tag{15}$$

Table 1 The admissible functions for different types of BCs [52, 53]

BCs	at $x = 0, a$	at $y = 0, b$	$X_m(x)$	$Y_n(y)$	(m, n)
SSSS-DB	$X_m = X_m^{''} = 0$	$Y_m = Y_m^{''} = 0$	$\sin \frac{m\pi x}{a}$	$\sin \frac{n\pi y}{b}$	$m, n = 1, 3, 5 \cdots$
SCSC-DB	$X_m = X_m^{'} = 0$	$Y_m = Y_m^{'} = 0$	$\sin \frac{m\pi x}{a}$	$\sin^2 \frac{n\pi y}{b}$	$m = 1, 3, 5 \cdots$ $n = 1, 2, 3 \cdots$
CCCC-DB	$X_m = X_m^{'} = 0$	$Y_m = Y_m^{'} = 0$	$\sin^2 \frac{m\pi x}{a}$	$\sin^2 \frac{n\pi y}{b}$	$m, n = 1, 2, 3 \cdots$

With the above BCs, general solutions are chosen in the following forms [32, 35]:

$$\overline{u}_0 = \sum_{m=1}^{M}\sum_{n=1}^{N} \overline{u}_{0mn} U_{1m}(x) U_{2n}(y) \quad \overline{v}_0 = \sum_{m=1}^{M}\sum_{n=1}^{N} \overline{v}_{0mn} V_{1m}(x) V_{2n}(y) \tag{16a}$$

$$\begin{gathered} \overline{\theta}_x = \sum_{m=1}^{M}\sum_{n=1}^{N} \overline{\theta}_{xmn} X_m^{'}(x) Y_n(y) \quad \overline{\theta}_y = \sum_{m=1}^{M}\sum_{n=1}^{N} \overline{\theta}_{ymn} X_m(x) Y_n^{'}(y) \\ \overline{w}_0 = \sum_{m=1}^{M}\sum_{n=1}^{N} \overline{w}_{0mn} X_m(x) Y_n(y) \end{gathered} \tag{16b}$$

in which $\overline{u}_{0mn}$, $\overline{v}_{0mn}$, $\overline{w}_{0mn}$, $\overline{\theta}_{xmn}$, $\overline{\theta}_{ymn}$ are unknown coefficients that need to be determined;

$$U_{1m}(x) = \sin \frac{2m\pi x}{a};\ U_{2n}(y) = \sin \frac{(2n-1)\pi y}{b};\ V_{1m}(x) = \sin \frac{(2m-1)\pi x}{a};\ V_{2n}(y) = \sin \frac{2n\pi y}{b};$$

with $m, n = 1, 2, 3 \cdots$.

Suggested functions $X_m(x)$, $Y_n(y)$ satisfy the geometric BCs given in Eqs. (13), (14), and (15) and describe approximate shapes of the deflected surface of the FGP plate. These functions for various types of BCs are tabulated in Table 1.

By substituting Eq. (16) into Eq. (12), we obtain:

$$\sum_{m=1}^{M}\sum_{n=1}^{N}\left(\overline{u}_{0mn}\tilde{l}_{mn}^{(11)} + \overline{v}_{0mn}\tilde{l}_{mn}^{(12)}\right) + \sum_{m=1}^{M}\sum_{n=1}^{N}\sum_{p=1}^{M}\sum_{q=1}^{N} \overline{w}_{0mn}\overline{w}_{0pq}\tilde{h}_{mnpq}^{(13)} = 0 \tag{17a}$$

$$\sum_{m=1}^{M}\sum_{n=1}^{N}\left(\overline{u}_{0mn}\tilde{l}_{mn}^{(21)} + \overline{v}_{0mn}\tilde{l}_{mn}^{(22)}\right) + \sum_{m=1}^{M}\sum_{n=1}^{N}\sum_{p=1}^{M}\sum_{q=1}^{N} \overline{w}_{0mn}\overline{w}_{0pq}\tilde{h}_{mnpq}^{(23)} = 0 \tag{17b}$$

$$\begin{aligned} &\sum_{m=1}^{M}\sum_{n=1}^{N}\left(\overline{w}_{0mn}\tilde{l}_{mn}^{(33)} + \overline{\theta}_{xmn}\tilde{l}_{mn}^{(34)} + \overline{\theta}_{ymn}\tilde{l}_{mn}^{(35)}\right) + \sum_{m=1}^{M}\sum_{n=1}^{N}\sum_{p=1}^{M}\sum_{q=1}^{N}\left(\overline{u}_{0mn}\overline{w}_{0pq}\tilde{h}_{mnpq}^{(31)} + \overline{v}_{0mn}\overline{w}_{0pq}\tilde{h}_{mnpq}^{(32)}\right) \\ &+ \sum_{m=1}^{M}\sum_{n=1}^{N}\sum_{p=1}^{M}\sum_{q=1}^{N}\sum_{r=1}^{M}\sum_{s=1}^{N} \overline{w}_{0mn}\overline{w}_{0pq}\overline{w}_{0rs}\tilde{p}_{mnpqrs}^{(33)} + q = 0 \end{aligned} \tag{17c}$$

$$\sum_{m=1}^{M}\sum_{n=1}^{N}\left(\overline{w}_{0mn}\tilde{l}_{mn}^{(43)} + \overline{\theta}_{xmn}\tilde{l}_{mn}^{(44)} + \overline{\theta}_{ymn}\tilde{l}_{mn}^{(45)}\right) = 0 \tag{17d}$$

$$\sum_{m=1}^{M}\sum_{n=1}^{N}\left(\overline{w}_{0mn}\tilde{l}_{mn}^{(53)} + \overline{\theta}_{xmn}\tilde{l}_{mn}^{(54)} + \overline{\theta}_{ymn}\tilde{l}_{mn}^{(55)}\right) = 0, \tag{17e}$$

in which the functions $\tilde{l}_{mn}^{(\,)}(x, y)$, $\tilde{h}_{mnpq}^{(\,)}(x, y)$, $\tilde{g}_{mnpqrx}^{(\,)}(x, y)$ are presented in Appendix A.

By employing the Galerkin method, multiplying each equation of Eqs. (17) with the corresponding eigenfunction and integrating over the domain of solution, the following equations are obtained:

$$\sum_{m=1}^{M}\sum_{n=1}^{N}\left(\overline{u}_{0mn}\tilde{L}^{(11)}_{mnij}+\overline{v}_{0mn}\tilde{L}^{(12)}_{mnij}\right)+\sum_{m=1}^{M}\sum_{n=1}^{N}\sum_{p=1}^{M}\sum_{q=1}^{N}\overline{w}_{0mn}\overline{w}_{0pq}\tilde{H}^{(13)}_{mnpqij}=0 \tag{18a}$$

$$\sum_{m=1}^{M}\sum_{n=1}^{N}\left(\overline{u}_{0mn}\tilde{L}^{(21)}_{mnij}+\overline{v}_{0mn}\tilde{L}^{(22)}_{mnij}\right)+\sum_{m=1}^{M}\sum_{n=1}^{N}\sum_{p=1}^{M}\sum_{q=1}^{N}\overline{w}_{0mn}\overline{w}_{0pq}\tilde{H}^{(23)}_{mnpqij}=0 \tag{18b}$$

$$\sum_{m=1}^{M}\sum_{n=1}^{N}\left(\overline{w}_{0mn}\tilde{L}^{(33)}_{mnij}+\overline{\theta}_{xmn}\tilde{L}^{(34)}_{mnij}+\overline{\theta}_{ymn}\tilde{L}^{(35)}_{mnij}\right)+\sum_{m=1}^{M}\sum_{n=1}^{N}\sum_{p=1}^{M}\sum_{q=1}^{N}\left(\overline{u}_{0mn}\overline{w}_{0pq}\tilde{H}^{(31)}_{mnpqij}+\overline{v}_{0mn}\overline{w}_{0pq}\tilde{H}^{(32)}_{mnpqij}\right)$$
$$+\sum_{m=1}^{M}\sum_{n=1}^{N}\sum_{p=1}^{M}\sum_{q=1}^{N}\sum_{r=1}^{M}\sum_{s=1}^{N}\overline{w}_{0mn}\overline{w}_{0pq}\overline{w}_{0rs}\tilde{P}^{(33)}_{mnpqrsij}+\tilde{F}_{ij}=0 \tag{18c}$$

$$\sum_{m=1}^{M}\sum_{n=1}^{N}\left(\overline{w}_{0mn}\tilde{L}^{(43)}_{mnij}+\overline{\theta}_{xmn}\tilde{L}^{(44)}_{mnij}+\overline{\theta}_{ymn}\tilde{L}^{(45)}_{mnij}\right)=0 \tag{18d}$$

$$\sum_{m=1}^{M}\sum_{n=1}^{N}\left(\overline{w}_{0mn}\tilde{L}^{(53)}_{mnij}+\overline{\theta}_{xmn}\tilde{L}^{(54)}_{mnij}+\overline{\theta}_{ymn}\tilde{L}^{(55)}_{mnij}\right)=0, \tag{18e}$$

in which the coefficients $\tilde{L}^{(\,)}_{mnij}$, $\tilde{H}^{(\,)}_{mnpqij}$, $\tilde{P}^{(\,)}_{mnpqrsij}$, $\tilde{F}_{ij}$ are presented in Appendix B.

The solution of nonlinear algebraic Eq. (18) is the displacement vector $\left\{\overline{u}_{0mn};\ \overline{v}_{0mn}\ ;\overline{w}_{0mn};\ \overline{\theta}_{xmn};\ \overline{\theta}_{ymn}\right\}$.

4.2 Stress-based approach

Introducing Airy stress function $\varphi(x,\ y)$ defined by:

$$N_x=\varphi_{,yy};\quad N_y=\varphi_{,xx};\quad N_{xy}=-\varphi_{,xy}. \tag{19}$$

It can be observed that Eqs. (12a) and (12b) are automatically satisfied.

Equation (12c) is rewritten in terms of displacements and stress function as follows:

$$\begin{aligned}\tilde{A}^{s}_{44}\overline{w}_{0,yy}+\tilde{A}^{s}_{44}\overline{w}_{0,xx}+\tilde{A}^{s}_{44}\overline{\theta}_{x,x}+\tilde{A}^{s}_{44}\overline{\theta}_{y,y}+\varphi_{,yy}\overline{w}_{0,xx}-2\varphi_{,xy}\overline{w}_{0,xy}+\varphi_{,xx}\overline{w}_{0,yy}\\ -K_w\overline{w}_0+K_{sx}\overline{w}_{0,xx}+K_{sy}\overline{w}_{0,yy}+q=0.\end{aligned} \tag{20}$$

Besides, the geometrical compatibility equation for the rectangular plate is expressed as [54]:

$$\varepsilon^0_{x,yy}+\varepsilon^0_{y,xx}-\gamma^0_{xy,xy}=\overline{w}^2_{0,xy}-\overline{w}_{0,xx}\overline{w}_{0,yy}. \tag{21}$$

Based on Eqs. (9) and (19), the in-plane strains are determined in terms of in-plane stress resultants and stress function:

$$\begin{aligned}\varepsilon^0_x&=\frac{\tilde{A}_{11}}{\tilde{A}^2_{11}-\tilde{A}^2_{12}}N_x-\frac{\tilde{A}_{12}}{\tilde{A}^2_{11}-\tilde{A}^2_{12}}N_y=\frac{\tilde{A}_{11}}{\tilde{A}^2_{11}-\tilde{A}^2_{12}}\varphi_{,yy}-\frac{\tilde{A}_{12}}{\tilde{A}^2_{11}-\tilde{A}^2_{12}}\varphi_{,xx},\\ \varepsilon^0_y&=\frac{\tilde{A}_{11}}{\tilde{A}^2_{11}-\tilde{A}^2_{12}}N_y-\frac{\tilde{A}_{12}}{\tilde{A}^2_{11}-\tilde{A}^2_{12}}N_x=\frac{\tilde{A}_{11}}{\tilde{A}^2_{11}-\tilde{A}^2_{12}}\varphi_{,xx}-\frac{\tilde{A}_{12}}{\tilde{A}^2_{11}-\tilde{A}^2_{12}}\varphi_{,yy},\\ \gamma^0_{xy}&=\frac{1}{\tilde{A}_{66}}N_{xy}=-\frac{1}{\tilde{A}_{66}}\varphi_{,xy}.\end{aligned} \tag{22}$$

Substituting Eq. (22) in compatibility Eq. (21), we obtain:

$$\varphi_{,xxxx}+2\varphi_{,xxyy}+\varphi_{,yyyy}=\tilde{D}\left(w^2_{0,xy}-\overline{w}_{0,xx}\overline{w}_{0,yy}\right), \tag{23}$$

where $\tilde{D}=\tilde{A}_{11}\left(1-\nu^2\right)$.

The governing equations including Eqs. (12c), (12d) and (12e) and Eq. (15) are used to investigate the nonlinear bending behavior of FGP plates. This is a system of four nonlinear equations with 4 independent unknowns $\overline{w}_0, \overline{\theta}_x, \overline{\theta}_y, \varphi$.

Herein, three cases of boundary conditions (BCs) similar to the displacement-based approach are considered:

– **Case 1b** (SSSS-SB): All four edges of plates are simply supported and immovable. The associated BCs are:

$$\overline{u}_n = \overline{w}_0 = \overline{\theta}_s = 0,\ N_{ns} = 0,\ M_n = 0 \tag{24}$$

– **Case 2b** (CCCC-SB): All four edges of the plates are clamped and immovable. The associated BCs are:

$$\overline{u}_n = \overline{w}_0 = \overline{\theta}_n = \overline{\theta}_s = 0,\ N_{ns} = 0 \tag{25}$$

– **Case 3b** (SCSC-SB): Two opposite edges are simply supported, the others are clamped and immovable. The associated BCs are:

$$\begin{aligned} &\text{At } x = 0, a\text{: } \overline{u}_0 = \overline{w}_0 = \overline{\theta}_y = 0,\ N_{xy} = 0,\ M_x = 0 \\ &\text{At } y = 0, b\text{: } \overline{v}_0 = \overline{w}_0 = \overline{\theta}_x = \overline{\theta}_y = 0,\ N_{xy} = 0 \end{aligned} \tag{26}$$

The in-plane immovable BCs, such as $\overline{u}_0 = 0$ (at $x = 0, a$) and $\overline{v}_0 = 0$ (at $y = 0, b$), are satisfied in the average sense [55, 56]:

$$\int_0^b \int_0^a \overline{u}_{0,x} \mathrm{d}x\mathrm{d}y = 0; \quad \int_0^b \int_0^a \overline{v}_{0,y} \mathrm{d}x\mathrm{d}y = 0 \tag{27}$$

In general, for all three abovementioned BCs, the stress function is chosen in the form

$$\varphi = \overline{\varphi}(x, y) + N_{x0}\frac{y^2}{2} + N_{y0}\frac{x^2}{2}, \tag{28}$$

in which N_{x0}, N_{y0} are in-plane support reactions in the plate edges due to they are in-plane immoveable.

From Eq. (27), we obtain in-plane support reactions as follows:

$$\begin{aligned} N_{x0} &= \frac{1}{ab}\int_0^b \int_0^a \left(-\overline{\varphi}_{,yy} + \frac{\tilde{A}_{11}}{2}\overline{w}_{0,x}^2 + \frac{\tilde{A}_{12}}{2}\overline{w}_{0,y}^2\right)\mathrm{d}x\mathrm{d}y, \\ N_{y0} &= \frac{1}{ab}\int_0^b \int_0^a \left(-\overline{\varphi}_{,xx} + \frac{\tilde{A}_{12}}{2}\overline{w}_{0,x}^2 + \frac{\tilde{A}_{11}}{2}\overline{w}_{0,y}^2\right)\mathrm{d}x\mathrm{d}y. \end{aligned} \tag{29}$$

According to the stress-based approach, displacements $\overline{w}_0, \overline{\theta}_x, \overline{\theta}_y$ are also chosen in the form of series expansion similar to the displacement-based approach presented in Eq. (16b). Substituting these displacements in two Eqs. (12d) and (12e), the obtained results are also Eqs. (17d), (17e), (18d) and (18e). Thus, in the next, the stress function φ will be determined in terms of $\overline{w}_0$ to substitute in Eq. (20), which leads to three equations in terms of only three unknowns $\overline{w}_0, \overline{\theta}_x, \overline{\theta}_y$.

Substituting the assumed deflection $\overline{w}_0$ from Eq. (16b) in Eq. (23), the obtained stress function $\overline{\varphi}$ is obtained as follows:

4.2.1 For boundary condition SSSS-SB

$$\overline{\varphi} = \sum_p \sum_q \sum_r \sum_s \overline{w}_{0pq}\overline{w}_{0rs} \begin{Bmatrix} \chi_1 \cos(\alpha_p - \alpha_r)x \cos(\lambda_q - \lambda_s)y \\ +\chi_2 \cos(\alpha_p + \alpha_r)x \cos(\lambda_q + \lambda_s)y \\ +\chi_3 \cos(\alpha_p - \alpha_r)x \cos(\lambda_q + \lambda_s)y \\ +\chi_4 \cos(\alpha_p + \alpha_r)x \cos(\lambda_q - \lambda_s)y \end{Bmatrix}, \tag{30}$$

in which $\alpha_p = \frac{p\pi}{a}, \alpha_r = \frac{r\pi}{a}$; $\lambda_q = \frac{q\pi}{b}, \lambda_s = \frac{s\pi}{b}$; coefficients $\chi_1, \chi_2, \chi_3, \chi_4$ are presented in Appendix C.

4.2.2 For boundary condition SCSC-SB

$$\overline{\varphi} = \sum_p \sum_q \sum_r \sum_s \overline{w}_{0pq}\overline{w}_{0rs} \begin{bmatrix} \chi_1 \cos(\alpha_p - \alpha_r)x \cos 2(\lambda_q - \lambda_s)y \\ +\chi_2 \cos(\alpha_p + \alpha_r)x \cos 2(\lambda_q + \lambda_s)y \\ +\chi_3 \cos(\alpha_p - \alpha_r)x \cos 2(\lambda_q + \lambda_s)y \\ +\chi_4 \cos(\alpha_p + \alpha_r)x \cos 2(\lambda_q - \lambda_s)y \\ +\chi_5 \cos(\alpha_p - \alpha_r)x \cos 2\lambda_s y + \chi_6 \cos(\alpha_p + \alpha_r)x \cos 2\lambda_s y \end{bmatrix}, \tag{31}$$

in which the coefficients χ_1 to χ_6 are presented in Appendix D.

4.2.3 For boundary condition CCCC-SB

$$\overline{\varphi} = \sum_p \sum_q \sum_r \sum_s \overline{w}_{0pq}\overline{w}_{0rs} \begin{bmatrix} \chi_1 \cos 2(\alpha_p - \alpha_r)x \cos 2(\lambda_q - \lambda_s)y \\ +\chi_2 \cos 2(\alpha_p + \alpha_r)x \cos 2(\lambda_q + \lambda_s)y \\ +\chi_3 \cos 2(\alpha_p - \alpha_r)x \cos 2(\lambda_q + \lambda_s)y \\ +\chi_4 \cos 2(\alpha_p + \alpha_r)x \cos 2(\lambda_q - \lambda_s)y + \chi_5 \cos 2\alpha_p x \cos 2\lambda_s y \\ +\chi_6 \cos 2\alpha_p x \cos 2(\lambda_q - \lambda_s)y + \chi_7 \cos 2\alpha_p x \cos 2(\lambda_q + \lambda_s)y \\ +\chi_8 \cos 2(\alpha_p - \alpha_r)x \cos 2\lambda_s y + \chi_9 \cos 2(\alpha_p + \alpha_r)x \cos 2\lambda_s y \end{bmatrix}, \tag{32}$$

in which the coefficients $\chi_1 \div \chi_9$ are presented in Appendix E.

Substituting Eqs. (31), (32) and (33) determining $\overline{\varphi}$ in Eq. (30), the in-plane support reactions of the plate can be expressed in the form:

$$N_{x0} = \sum_p \sum_q \sum_r \sum_s \overline{w}_{0pq}\overline{w}_{0rs}\zeta^{(1)}_{pqrs}; N_{y0} = \sum_p \sum_q \sum_r \sum_s \overline{w}_{0pq}\overline{w}_{0rs}\zeta^{(2)}_{pqrs} \tag{33}$$

where the coefficients $\zeta^{(1)}_{pqrs}$, $\zeta^{(2)}_{pqrs}$ are presented in Appendix F.

Substituting $\overline{\varphi}$ and N_{x0}, N_{y0} in Eq. (28) to get the stress function $\varphi(x, y)$, then substituting $\varphi(x, y)$ in Eq. (20), we obtain:

$$\sum_m \sum_n \left(\overline{w}_{0mn}\tilde{l}^{(33)}_{mn} + \overline{\theta}_{xmn}\tilde{l}^{(34)}_{mn} + \overline{\theta}_{ymn}\tilde{l}^{(35)}_{mn}\right) + \sum_m \sum_n \sum_p \sum_q \sum_r \sum_s \overline{w}_{0mn}\overline{w}_{0pq}\overline{w}_{0rs}\tilde{g}^{(33)}_{mnpqrs} + q = 0, \tag{34}$$

in which the functions $\tilde{g}^{(3)}_{mnpqrs}(x, y)$ are presented in Appendix G, $\tilde{l}^{(\,)}_{mn}(x, y)$. They are the same as in the displacement-based approach and presented in Appendix A.

Finally, three Equation (18d), (18e), and (34) in terms of $\overline{w}_0, \overline{\theta}_x, \overline{\theta}_y$ have been obtained.

Multiplying each of Eqs. (34) with the corresponding eigenfunction and integrating over the domain of solution, the following equations are obtained:

$$\sum_m \sum_n \left(\overline{w}_{0mn}\tilde{L}^{(33)}_{mnij} + \overline{\theta}_{xmn}\tilde{L}^{(34)}_{mnij} + \overline{\theta}_{ymn}\tilde{L}^{(35)}_{mnij}\right) + \sum_m \sum_n \sum_p \sum_q \sum_r \sum_s \overline{w}_{0mn}\overline{w}_{0pq}\overline{w}_{0rs}\tilde{G}^{(33)}_{mnpqrsij} + \tilde{F}_{ij} = 0, \tag{35}$$

in which $\tilde{G}^{(33)}_{mnpqrsij} = \int_0^a \int_0^b \tilde{g}^{(33)}_{mnpqrs} X_i Y_j dxdy; \tilde{L}^{(\,)}_{mnij}$, $\tilde{F}_{ij}$ are similar to the displacement approach and are presented in Appendix B.

The roots of the set of algebraic nonlinear equations including (18d)–(18e) and (35) are the coefficients $\left\{\overline{w}_{0mn}; \overline{\theta}_{xmn}; \overline{\theta}_{ymn}\right\}$, from which we can determine displacements, strains, stresses, and stress resultants for nonlinear bending analysis of FGP plates.

For linear analysis, the set of algebraic linear equations is obtained by neglecting nonlinear strains in Eq. (7), $\tilde{H}^{(\,)}_{mnpqij}$, and $\tilde{P}^{(\,)}_{mnpqrsij}$ in Eq. (18c), or $\tilde{G}^{(33)}_{mnpqrsij}$ in Eq. (35).

Table 2 Non-dimensional central deflection $\overline{w}$ of square isotropic SCSC plate subjected to a uniform pressure $q_0 = PE_1h^4/a^4$

P	Azizian and Dawe [60]	Lei [59]	Present-SB	Present-DB	Discre *δ (%)
0.9158	0.0199	0.0199	0.0198	0.0198	0.23
4.5788	0.0988	0.0984	0.0982	0.0981	0.11
6.8681	0.1469	0.1455	0.1461	0.1459	0.17
9.1575	0.1936	0.1904	0.1929	0.1922	0.35

*Discrepancies between two approaches

5 Numerical results and discussion

The solutions of Eqs. (18a)–(18e) for the displacement-based approach and Eqs. (18d), (18e) and (35) for the stress-based approach have been carried out using $m \times n$ terms of double series. The convergence of the solution has been examined in detail for deflection and bending moments. For these double series, the number of terms is limited to 4×4 for acceptable accuracy and computational capability of the personal computer.

In this section, numerical examples are implemented by using the homemade Matlab's code to investigate the nonlinear bending behavior of FGP plates. Unless otherwise stated, nonlinear analysis is employed for all cases. For convenience, the following non-dimensional parameters are expressed in the form [57, 58]

$$\overline{w} = \frac{1}{h}\overline{w}_0\left(\frac{a}{2}, \frac{b}{2}\right);\ K_0 = \frac{K_w a^4}{E_0 h^3};\ J_0 = \frac{K_{sx}a^2}{E_0 h^3 \nu} = \frac{K_{sy}b^2}{E_0 h^3 \nu};\ E_0 = 1.0\ \text{GPa};\ P = \frac{q_0 a^4}{E_1 h^4}. \tag{36}$$

5.1 Validation study

To the knowledge of the authors, there are not any available results of nonlinear bending analysis of FGP plates in the literature. Therefore, a comparison study is conducted with isotropic plate (a particular case of porous materials—$e_0 = 0$).

5.1.1 Example 1

The square isotropic plate (SCSC) having two opposite edges simply supported ($x = 0$ and a) and remaining edges clamped is considered. The plate ($h/a = 0.05$) is subjected to uniform pressure q_0. Material parameters are given by Young's modulus $E = 0.3 \times 10^7$psi and Poisson ratio $\nu = 0.3$. Table 2 presents nonlinear non-dimensional central deflection of an isotropic plate with increasing load parameters P. The results are given by both approaches (displacement-based referred to as DB, stress-based referred to as SB) are compared with those of Lei [59] using the boundary element method, and Azizian và Dawe [60] using the finite strip method. Similarities between the present two approaches and slightly discrepancies in comparison with Lei, and Azizian and Dawe results can be found.

5.1.2 Example 2

The square plate ($a/h = 10$) made of isotropic material with Young's modulus $E = E_c = 322.27$ GPa (Si_3N_4) and Poisson ration $\nu = 0.28$ is subjected to uniform pressure $q_0 = P\frac{E_m h^4}{a^4}$ in which $E_m = 207.78$ GPa (SUS304).

Non-dimensional central deflections $\overline{w}$ calculated by present approaches and compared with results of Talha and Singh [61] using finite element method and HSDT. Results presented in Table 3 for three BCs including SSSS, SCSC, and CCCC with increasing values of load parameters. Almost identical results between the present two approaches and slightly discrepancies (lower than 2,5%) in comparison with Talha and Singh results [61] can be observed. Thus, the accuracy and reliability of the proposed approaches have been confirmed through the above two validated examples.

Table 3 Non-dimensional central deflection $\overline{w}$ of square isotropic SCSC plate under different BCs and subjected to a uniform pressure

Methods	$P = 4$	$P = 8$	$P = 12$	$P = 16$	$P = 20$	$P = 40$
SSSS						
Talha and Singh [61]	0.1200	0.2251	0.3185	0.3911	0.4597	0.6984
Present-DB	0.1189	0.2254	0.3160	0.3927	0.4583	0.6908
Present-SB	0.1188	0.2253	0.3156	0.3918	0.4569	0.6845
Discrepancy* δ (%)	0.02	0.06	0.13	0.22	0.32	0.92
SCSC						
Talha và Singh [61]	0.0602	0.1193	0.1764	0.2306	0.2811	0.4942
Present-DB	0.0594	0.1179	0.1745	0.2286	0.2800	0.4953
Present-SB	0.0595	0.1180	0.1748	0.2293	0.2812	0.5003
Discrepancy* δ (%)	0.02	0.09	0.18	0.30	0.43	1.01
CCCC						
Talha và Singh [61]	0.0405	0.0808	0.1207	0.1598	0.1981	0.3698
Present-DB	0.0395	0.0788	0.1177	0.1560	0.1936	0.3681
Present-SB	0.0395	0.0788	0.1178	0.1563	0.1942	0.3714
Discrepancy* δ (%)	0.01	0.05	0.11	0.19	0.28	0.89

*Discrepancies between two approaches

Table 4 Non-dimensional central deflections $\overline{w}$ of square FGP plates (Type 2) obtained by increasing numbers of terms of double trigonometric series

BCs	$m, n = 1$	$m, n = 2$	$m, n = 3$	$m, n = 4$
SSSS-DB	0.4644	0.4447	0.4466	0.4461
SCSC-DB	0.2812	0.2666	0.2755	0.2750
CCCC-DB	0.1974	0.1837	0.1946	0.1931
SSSS-SB	0.4627	0.4436	0.4458	0.4452
SCSC-SB	0.2782	0.2675	0.2769	0.2766
CCCC-SB	0.1961	0.1842	0.1957	0.1942

5.2 Parametric studies

To perform nonlinear analysis, the FGP plate made of metal foam ($E_1 = 200$ GPa, $\nu = 1/3$) with/without elastic foundation under uniform pressure $q_0 = PE_1h^4/a^4$ is considered. The effects of porosity distribution patterns, porosity coefficients, geometrical, and elastic foundation parameters on the nonlinear bending response of the FGP plate are investigated in turn.

Table 4 shows nonlinear non-dimensional central deflections of square FGP plates with nonuniform symmetric porosity distribution (the same porosity coefficient) without elastic foundation (Type 2, $h = 0.1$ m, $a/h = 10$, $b/a = 1$, $e_0 = 0.5$, $P = 10$, $K_0 = J_0 = 0$). The plate subjected to different boundary conditions (for displacement-based approach referred to as SSSS-DB, SCSC-DB, CCCC-DB; for stress-based approach referred to as SSSS-SB, SCSC-SB, CCCC-SB). Various numbers of terms of double trigonometric series are used for calculation. It is observed that the number of terms can be limited to 4×4 for the next analysis (the difference between 3×3 and 4×4 terms is only 0.79% for CCCC-DB boundary conditions).

Table 5 presents linear and nonlinear non-dimensional central deflections and bending moment M_x of simply supported FGP plate ($h = 0.1$ m, $a/h = 10$, $b/a = 1$, $e_0 = 0.5$, $P = 10$, $K_0 = J_0 = 0$). The plate is subjected to uniform pressure in the range of $P = 5$ to $P = 30$. Three porosity distribution patterns (the same porosity coefficient) including uniform (Type 1), nonuniform symmetric (Type 2), and nonuniform asymmetric (Type 3) are considered. Linear (LN), nonlinear (NL) load–deflection curves ($P - \overline{w}$), and load-bending moment curves ($P - M_x$) are plotted in Figs. 3 and 4, in which the straight lines represent linear analysis, and the curves represent nonlinear analysis.

Results from Table 5 and Figs. 3 and 4 indicate that:

- As expected, the non-dimensional central deflections, bending moments obtained by linear analysis are always higher than by nonlinear analysis, and higher applied load causes a bigger gap between the two analyses.
- In linear analysis, the load–deflection curves and load-bending moment curves obtained by using two approaches (DB and SB) are completely identical. Only porosity distribution patterns affect deflection:

Table 5 Non-dimensional central deflections $\overline{w}$ and bending moment M_x of simply supported square FGP plates under increasing load parameters P

P	BCs	Type 1	Type 2	Type 3
Non-dimensional central deflections $\overline{w}$				
5	SSSS-DB	0.3025 (0.3454)*	0.2593 (0.2820)	0.2970 (0.3379)
	SSSS-SB	0.3023 (0.3454)	0.2592 (0.2820)	0.2968 (0.3379)
10	SSSS-DB	0.4973 (0.6908)	0.4466 (0.5640)	0.4897 (0.6758)
	SSSS-SB	0.4958 (0.6908)	0.4458 (0.5640)	0.4883 (0.6758)
15	SSSS-DB	0.6325 (1.0362)	0.5826 (0.8460)	0.6238 (1.0137)
	SSSS-SB	0.6288 (1.0362)	0.5803 (0.8460)	0.6203 (1.0137)
30	SSSS-DB	0.8945 (2.0724)	0.8502 (1.6920)	0.8838 (2.0275)
	SSSS-SB	0.8810 (2.0724)	0.8410 (1.6920)	0.8708 (2.0275)
Bending moment M_x (MNm/m)				
5	SSSS-DB	4.2317 (4.8963)	4.4656 (4.8963)	4.2484 (4.8963)
	SSSS-SB	4.2141 (4.8963)	4.4546 (4.8963)	4.2315 (4.8963)
10	SSSS-DB	6.8129 (9.7926)	7.5763 (9.7926)	6.8625 (9.7926)
	SSSS-SB	6.7165 (9.7926)	7.5093 (9.7926)	6.7684 (9.7926)
15	SSSS-DB	8.5074 (14.6888)	9.7371 (14.6888)	8.5837 (14.6888)
	SSSS-SB	8.2784 (14.6888)	9.5669 (14.6888)	8.3591 (14.6888)
30	SSSS-DB	11.5594 (29.3777)	13.7264 (29.3777)	11.6863 (29.3777)
	SSSS-SB	10.7467 (29.3777)	13.0582 (29.3777)	10.8836 (29.3777)

*The numbers in the parenthesis denote the linear analysis

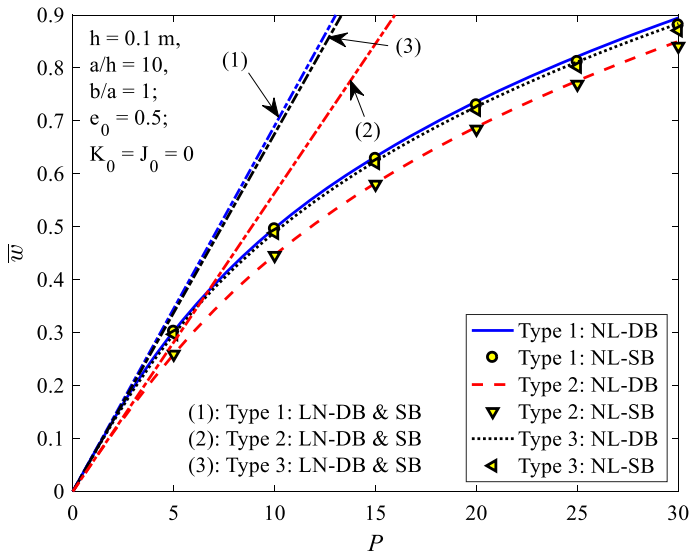

Fig. 3 Non-dimensional central deflection $\overline{w}$ of FGP plate versus load parameters P with three porosity distribution patterns

Nonuniform symmetric porosity distribution (Type 2) produces the lowest deflection, and two remaining uniform porosity distribution (Type 1) and nonuniform asymmetric porosity distribution (Type 3) produce almost similar deflections (Type 1 produces larger deflection than Type 3). Meanwhile, bending moments do not depend on porosity distribution patterns as expected.

– In nonlinear analysis, the nonlinear central deflection of the FGP-Type 2 plate is the smallest, but the bending moment is the highest; the response of FGP-Type 1 plates is opposite, the nonlinear central deflection is highest, and bending moment is smallest. There is a slight difference in obtained results between the FGP-Type 1 plate and the FGP-Type 3 plate. The gap between load–deflection curves obtained by using two approaches (DB and SB) increases with increasing load parameter P. This trend is similar to load-bending moment curves, but with the same level of load parameters, the gap between load-bending moment curves is bigger than between load–deflection curves. For example, for FGP-Type 1, when $P = 5$, the discrepancies between two approaches for deflection and bending moment are 0.08% and 0.42%, respectively; when $P = 30$, the corresponding discrepancies are 1.53% và 7.56%.

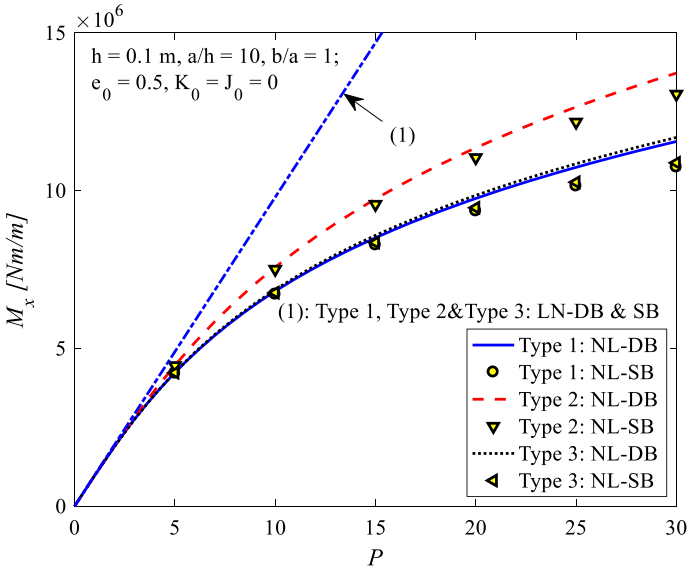

Fig. 4 Bending moment M_x (Nm/m) of FGP plate versus load parameters P with three porosity distribution patterns

Table 6 Non-dimensional central deflection $\overline{w}$ simply supported square FGP plates (Type 2) with and without elastic foundation

(K_0, J_0)	P			
	5	10	15	30
SSSS-DB				
(0, 0)	0.2593	0.4466	0.5826	0.8502
(300, 0)	0.2483	0.4329	0.5687	0.8379
(300, 100)	0.2268	0.4047	0.5398	0.8119
SSSS-SB				
(0, 0)	0.2592	0.4458	0.5803	0.8410
(300, 0)	0.2482	0.4321	0.5665	0.8289
(300, 100)	0.2267	0.4040	0.5380	0.8039

The effect of Pasternak's foundation parameters K_0, J_0 on the nonlinear load–deflection curves of FGP is tabulated in Table 6 and illustrated graphically in Fig. 5. The FGP plates are subjected to different level of load parameters P with input data: Type 2, $h = 0.1$ m, $a/h = 10$, $b/a = 1$, $e_0 = 0.5$; three pairs of foundation parameters ($K_0 = 0$, $J_0 = 0$; $K_0 = 100$, $J_0 = 0$ và $K_0 = 300$, $J_0 = 100$) are considered. It can be seen that the presence of elastic foundation increases plate stiffness, resulting in a decrease of deflection. In addition, the influence of foundation parameter J_0 (shear stiffness coefficients) is more significant than K_0 (transverse stiffness coefficients).

Table 7 presents non-dimensional central deflection $\overline{w}$ of simply supported FGP plate ($h = 0.1$ m, $a/h = 10$, $b/a = 1$, $P = 10$, $K_0 = J_0 = 0$) with three different porosity distribution patterns and porosity coefficients. Figure 6 depicts the variation of non-dimensional central deflection versus porosity coefficient. It can be seen that under a given load parameter, the non-dimensional central deflection increases with the increase in the porosity coefficient for all porosity distribution patterns. This is due to the fact that the increasing porosity coefficient increases the size and amount of internal pores which results in a decrease in the FGP plate stiffness. Furthermore, the larger the porosity coefficient, the greater effect of porosity distribution patterns. Again, the effect of porosity distribution patterns on non-dimensional central deflection is indicated clearly. The FGP plate with nonuniform symmetric porosity distribution (FGP-Type 2) has the highest bending stiffness (causes the smallest deflection), and the FGP-Type 2 plate has the lowest bending stiffness (causes the biggest deflection).

The influences of side-to-thickness ratio *a/h*, aspect ratio *b/a*, and boundary conditions on the non-dimensional central deflection $\overline{w}$ of simply supported FGP-Type 2 plate are described in Tables 8 and 9, and Figs. 7 and 8, respectively. The nonlinear analysis is carried out by using both approaches DB and SB. From these figures, it can be seen that:

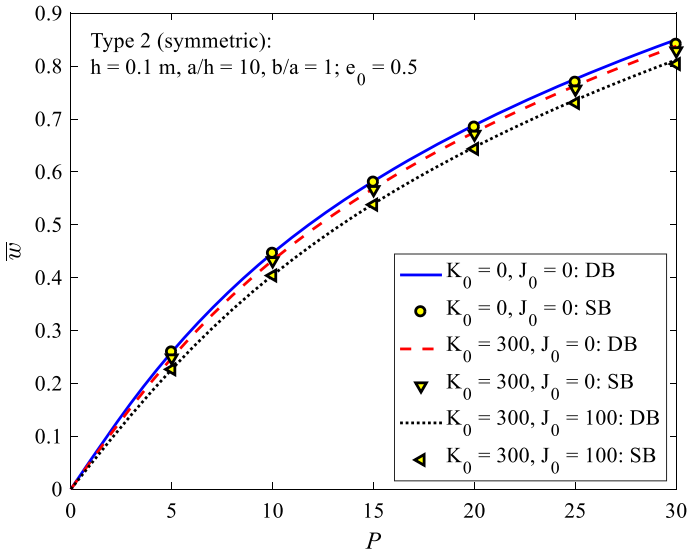

Fig. 5 Non-dimensional central deflection $\overline{w}$ of FGP plate versus load parameters P with different foundation parameters

Table 7 Non-dimensional central deflection $\overline{w}$ simply supported square FGP plates with different porosity distribution patterns and porosity coefficients

e_0	BCs	Type 1	Type 2	Type 3
0.1	SSSS-DB	0.3936	0.3871	0.3923
	SSSS-SB	0.3929	0.3865	0.3917
0.3	SSSS-DB	0.4380	0.4143	0.4339
	SSSS-SB	0.4370	0.4136	0.4330
0.5	SSSS-DB	0.4973	0.4466	0.4897
	SSSS-SB	0.4958)	0.4458	0.4883
0.9	SSSS-DB	0.7504	0.5380	0.7020
	SSSS-SB	0.7434	0.5367	0.6942

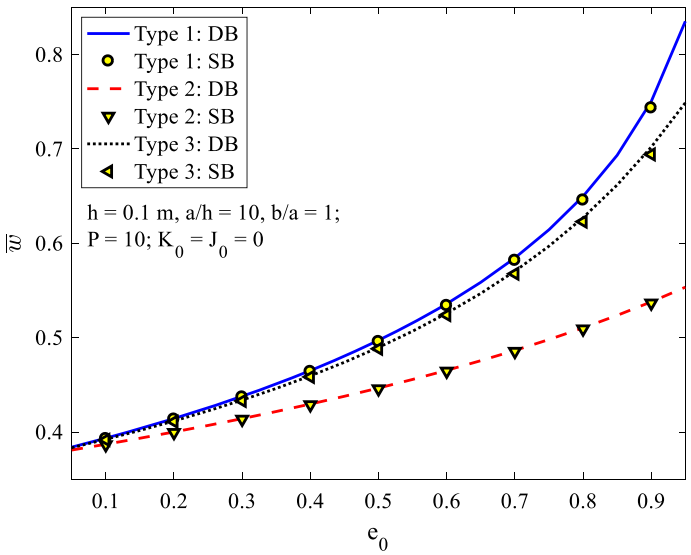

Fig. 6 Non-dimensional central deflection $\overline{w}$ of FGP plate versus porosity coefficient e_0 with three porosity distribution patterns

Table 8 Non-dimensional central deflection $\overline{w}$ of square FGP plate ($h = 0.1$ m, $b/a = 1$, $P = 10$, $K_0 = J_0 = 0$) with different side-to-thickness ratio *a/h* and BCs

BCs	*a/h*			
	5	10	30	50
SSSS-DB	0.4832	0.4466	0.4335	0.4324
SSSS-SB	0.4802	0.4458	0.4331	0.4320
SCSC-DB	0.3619	0.2755	0.2445	0.2419
SCSC-SB	0.3643	0.2769	0.2455	0.2429
CCCC-DB	0.2813	0.1946	0.1662	0.1639
CCCC-SB	0.2846	0.1957	0.1668	0.1645

Table 9 Non-dimensional central deflection $\overline{w}$ of square FGP plate ($h = 0.1$ m, $a/h = 10$, $P = 10$, $K_0 = J_0 = 0$) with different aspect ratio *b/a* and BCs

BCs	*b/a*			
	0.5	1	1.5	2
SSSS-DB	0.0944	0.4466	0.6482	0.7143
SSSS-SB	0.0944	0.4458	0.6435	0.7014
SCSC-DB	0.0348	0.2755	0.5656	0.6923
SCSC-SB	0.0348	0.2769	0.5687	0.6954
CCCC-DB	0.0339	0.1946	0.3169	0.3588
CCCC-SB	0.0339	0.1957	0.3216	0.3663

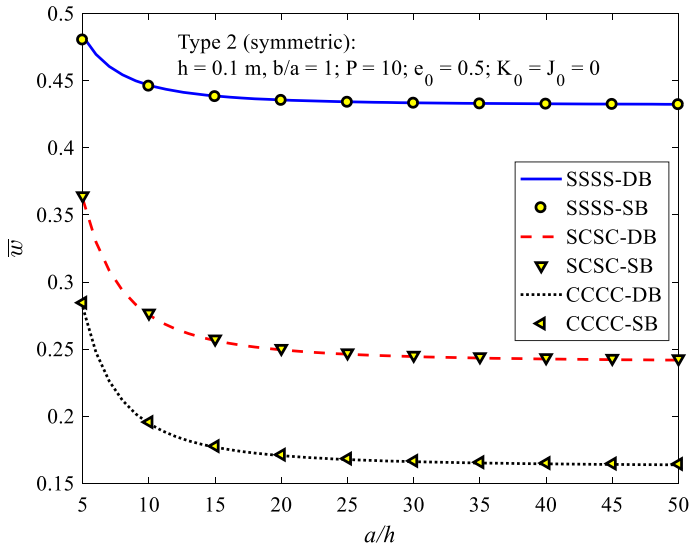

Fig. 7 Non-dimensional central deflection $\overline{w}$ of FGP plate versus side-to-thickness ratio *a/h* under different boundary conditions

– Among three considered boundary conditions, the maximum deflections are obtained for the SSSS plate and minimum deflections for the CCCC plate as expected.
– Non-dimensional central deflection decreases with the increase in the side-to-thickness ratio *a/h* and increases with the increase in aspect ratio *b/a* for all types of BCs.

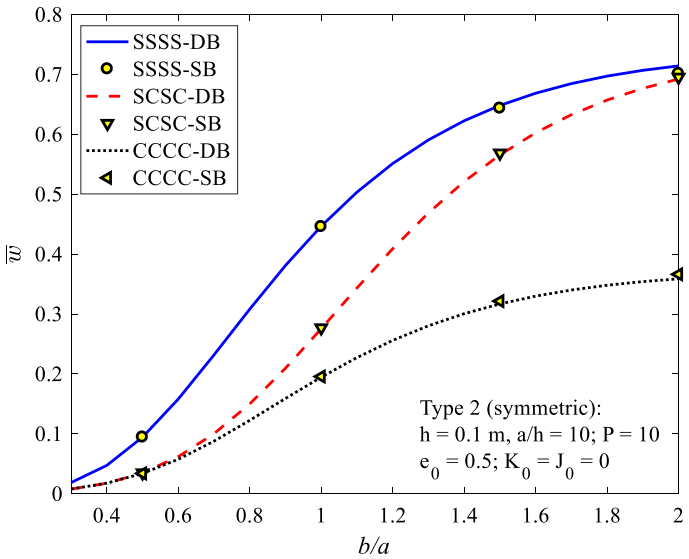

Fig. 8 Non-dimensional central deflection $\overline{w}$ of FGP plate versus aspect ratio *b/a* under different boundary conditions

6 Concluding remarks

In this paper, two approaches, namely displacement-based and stress-based, are proposed to analyze the nonlinear bending of FGP plates for the first time. The FGP plate consists of metal foam with three porosity distribution patterns, subjected to various boundary conditions are considered. The analytical solution is obtained by using FSDT, the neutral surface position concept, and the Galerkin method. The accuracy of the proposed approaches has been validated with available results in the literature. Parametric studies have been carried out to evaluate the effect of material and geometrical parameters of the plate as well as boundary conditions on the nonlinear behavior of the FGP plate. The major conclusion can be summarized as follows:

- By introducing the physical neutral surface concept, the stretching-bending coupling effect is eliminated, and the governing equations for analyzing the nonlinear bending response in the simple form are obtained. Both displacement-based and stress-based approaches are proposed to find the analytical solution in double trigonometric series form satisfying various boundary conditions.
- The nonlinear analysis results are always lower than linear analysis results. In linear analysis, the load–deflection curves and load-bending moment curves obtained by using the two approaches are completely identical. In nonlinear analysis, there are slight discrepancies between the results calculated by using the two approaches. With SSSS boundary conditions, the results obtained by using the stress-based approach are lower than those obtained by the displacement-based approach; with the remaining two types of boundary conditions (SCSC, CCCC), the obtained results are opposite. This is probably due to the influence of the constraint numbers of boundary conditions on the nonlinear analysis.
- The porosity distribution patterns play an important role in the nonlinear bending behavior of FGP plates. The FGP-Type 2 plate (nonuniform symmetric porosity distribution) produces the smallest non-dimensional deflection (i.e., the highest bending stiffness), the FGP-Type 1 plate (uniform porosity distribution) produces the highest non-dimensional deflection (i.e., the lowest bending stiffness).
- The non-dimensional central deflection of the FGP plate increases with increasing porosity coefficient. The larger the porosity coefficient, the more significant the influence of the porosity distribution pattern.
- The non-dimensional deflection decreases as the side-to-thickness ratio increases and the aspect ratio decreases.
- The foundation parameters have a significant effect on the nonlinear response of FGP plates. The effect of J_0 on the nonlinear deflection is more pronounced than that of K_0.
- The boundary conditions of FGP plates affect significantly the non-dimensional deflection. Increasing the constraints on the boundary conditions results in decreasing non-dimensional deflection.

Acknowledgements This research is funded by Hanoi University of Civil Engineering (HUCE) under Grant Number: 42-2021/KHXD-TĐ

Appendix A: The functions in Eq. (17)

$$\tilde{l}_{mn}^{(11)}(x,y) = \tilde{A}_{11}U_{1m}''U_{2n} + \tilde{A}_{66}U_{1m}U_{2n}''; \ \tilde{l}_{mn}^{(12)}(x,y) = \left(\tilde{A}_{12} + \tilde{A}_{66}\right)V_{1m}'V_{2n}';$$

$$\tilde{h}_{mnpq}^{(13)}(x,y) = \tilde{A}_{11}X_m'Y_nX_p''Y_q + \tilde{A}_{12}X_mY_n'X_p'Y_q' + \tilde{A}_{66}\left(X_m'Y_nX_pY_q'' + X_mY_n'X_p'Y_q'\right);$$

$$\tilde{l}_{mn}^{(21)}(x,y) = \left(\tilde{A}_{12} + \tilde{A}_{66}\right)U_{1m}'U_{2n}'; \ \tilde{l}_{mn}^{(22)}(x,y) = \tilde{A}_{11}V_{1m}V_{2n}'' + \tilde{A}_{66}V_{1m}''V_{2n};$$

$$\tilde{h}_{mnpq}^{(23)}(x,y) = \tilde{A}_{22}X_mY_n'X_pY_q'' + \tilde{A}_{12}X_m'Y_nX_p'Y_q' + \tilde{A}_{66}\left(X_m'Y_nX_p'Y_q' + X_mY_n'X_p''Y_q\right);$$

$$\tilde{l}_{mn}^{(33)}(x,y) = \tilde{A}_{44}^{s}X_mY_n'' + \tilde{A}_{55}^{s}X_m''Y_n - K_wX_mY_n + K_{sx}X_m''Y_n + K_{sy}X_mY_n'';$$

$$\tilde{l}_{mn}^{(34)}(x,y) = \tilde{A}_{55}^{s}X_m''Y_n; \ \tilde{l}_{mn}^{(35)}(x,y) = \tilde{A}_{44}^{s}X_mY_n'';$$

$$\tilde{h}_{mnpq}^{(31)}(x,y) = \tilde{A}_{11}U_{1m}'U_{2n}X_p''Y_q + \tilde{A}_{12}U_{1m}'U_{2n}X_pY_q'' + 2\tilde{A}_{66}U_{1m}U_{2n}'X_p'Y_q';$$

$$\tilde{h}_{mnpq}^{(32)}(x,y) = \tilde{A}_{12}V_{1m}V_{2n}'X_p''Y_q + \tilde{A}_{11}V_{1m}V_{2n}'X_pY_q'' + 2\tilde{A}_{66}V_{1m}'V_{2n}X_p'Y_q';$$

$$\tilde{p}_{mnpqrs}^{(33)}(x,y) = \frac{1}{2}\tilde{A}_{11}X_m'Y_nX_p'Y_qX_r''Y_s + \frac{1}{2}\tilde{A}_{12}X_mY_n'X_pY_q'X_r''Y_s + \frac{1}{2}\tilde{A}_{12}X_m'Y_nX_p'Y_qX_rY_s''$$
$$+\frac{1}{2}\tilde{A}_{11}X_mY_n'X_pY_q'X_rY_s'' + 2\tilde{A}_{66}X_m'Y_nX_pY_q'X_r'Y_s';$$

$$\tilde{l}_{mn}^{(43)}(x,y) = -\tilde{A}_{55}^{s}X_m'Y_n; \ \tilde{l}_{mn}^{(44)}(x,y) = \tilde{C}_{11}X_m'''Y_n - \tilde{A}_{55}X_m'Y_n + \tilde{C}_{66}X_m'Y_n'';$$

$$\tilde{l}_{mn}^{(45)}(x,y) = \left(\tilde{C}_{12} + \tilde{C}_{66}\right)X_m'Y_n''; \ \tilde{l}_{mn}^{(53)}(x,y) = -\tilde{A}_{44}^{s}X_mY_n'; \ \tilde{l}_{mn}^{(54)}(x,y) = \left(\tilde{C}_{12} + \tilde{C}_{66}\right)X_m''Y_n';$$

$$\tilde{l}_{mn}^{(55)}(x,y) = \tilde{C}_{66}X_m''Y_n' + \tilde{C}_{22}X_mY_n''' - \tilde{A}_{44}^{s}X_mY_n'$$

Appendix B: The coefficients in Eq. (18)

$$\left\{\tilde{L}_{mnij}^{(11)}, \tilde{L}_{mnij}^{(12)}, \tilde{H}_{mnpqij}^{(13)}\right\} = \int_0^a\int_0^b \left\{\tilde{l}_{mn}^{(11)}, \tilde{l}_{mn}^{(12)}, \tilde{h}_{mnpq}^{(13)}\right\}U_{1i}U_{2j}\mathrm{d}x\mathrm{d}y;$$

$$\left\{\tilde{L}_{mnij}^{(21)}, \tilde{L}_{mnij}^{(22)}, \tilde{H}_{mnpqij}^{(23)}\right\} = \int_0^a\int_0^b \left\{\tilde{l}_{mn}^{(21)}, \tilde{l}_{mn}^{(22)}, \tilde{h}_{mnpq}^{(23)}\right\}V_{1i}V_{2j}\mathrm{d}x\mathrm{d}y;$$

$$\left\{\tilde{L}_{mnij}^{(33)}, \tilde{L}_{mnij}^{(34)}, \tilde{L}_{mnij}^{(35)}, \tilde{H}_{mnpqij}^{(31)}, \tilde{H}_{mnpqij}^{(32)}, \tilde{P}_{mnpqrsij}^{(33)}\right\} = \int_0^a\int_0^b \left\{\tilde{l}_{mn}^{(33)}, \tilde{l}_{mn}^{(34)}, \tilde{l}_{mn}^{(35)}, \tilde{h}_{mnpq}^{(31)}, \tilde{h}_{mnpq}^{(32)}, \tilde{p}_{mnpqrs}^{(33)}\right\}X_iY_j\mathrm{d}x\mathrm{d}y;$$

$$\tilde{F}_{ij} = \int_0^a\int_0^b qX_iY_j\mathrm{d}x\mathrm{d}y;$$

$$\left\{\tilde{L}_{mnij}^{(43)}, \tilde{L}_{mnij}^{(44)}, \tilde{L}_{mnij}^{(45)}\right\} = \int_0^a\int_0^b \left\{\tilde{l}_{mn}^{(11)}, \tilde{l}_{mn}^{(12)}, \tilde{h}_{mnpq}^{(13)}, \tilde{l}_{mn}^{(43)}, \tilde{l}_{mn}^{(44)}, \tilde{l}_{mn}^{(45)}\right\}X_i'Y_j\mathrm{d}x\mathrm{d}y;$$

$$\left\{\tilde{L}_{mnij}^{(53)}, \tilde{L}_{mnij}^{(54)}, \tilde{L}_{mnij}^{(55)}\right\} = \int_0^a\int_0^b \left\{\tilde{l}_{mn}^{(11)}, \tilde{l}_{mn}^{(12)}, \tilde{h}_{mnpq}^{(13)}, \tilde{l}_{mn}^{(53)}, \tilde{l}_{mn}^{(54)}, \tilde{l}_{mn}^{(55)}\right\}X_iY_j'\mathrm{d}x\mathrm{d}y$$

Appendix C: The coefficients in Eq. (30) for SSSS-SB boundary condition

$$\chi_1 = \frac{\frac{\tilde{D}}{4}\left(\alpha_p\alpha_r\lambda_q\lambda_s - \alpha_p^2\lambda_s^2\right)}{\left[\left(\alpha_p - \alpha_r\right)^2 + \left(\lambda_q - \lambda_s\right)^2\right]^2};\ (\text{with } p = r \text{ và } q = s:\ \chi_1 = 0);$$

$$\chi_2 = \frac{\frac{\tilde{D}}{4}\left(\alpha_p\alpha_r\lambda_q\lambda_s - \alpha_p^2\lambda_s^2\right)}{\left[\left(\alpha_p + \alpha_r\right)^2 + \left(\lambda_q + \lambda_s\right)^2\right]^2};\ \chi_3 = \frac{\frac{\tilde{D}}{4}\left(\alpha_p\alpha_r\lambda_q\lambda_s + \alpha_p^2\lambda_s^2\right)}{\left[\left(\alpha_p - \alpha_r\right)^2 + \left(\lambda_q + \lambda_s\right)^2\right]^2};$$

$$\chi_4 = \frac{\frac{\tilde{D}}{4}\left(\alpha_p\alpha_r\lambda_q\lambda_s + \alpha_p^2\lambda_s^2\right)}{\left[\left(\alpha_p + \alpha_r\right)^2 + \left(\lambda_q - \lambda_s\right)^2\right]^2}$$

Appendix D: The coefficients in Eq. (31) for SCSC-SB boundary condition

$$\chi_1 = \frac{\frac{\tilde{D}}{4}\left(\alpha_p\alpha_r\lambda_q\lambda_s - \alpha_p^2\lambda_s^2\right)}{\left[\left(\alpha_p - \alpha_r\right)^2 + 4\left(\lambda_q - \lambda_s\right)^2\right]^2};(\text{with } p = r \text{ và } q = s:\chi_1 = 0);$$

$$\chi_2 = \frac{\frac{\tilde{D}}{4}\left[\alpha_p\alpha_r\lambda_q\lambda_s + \alpha_p^2\lambda_s^2\right]}{\left[\left(\alpha_p + \alpha_r\right)^2 + 4\left(\lambda_q + \lambda_s\right)^2\right]^2};\ \chi_3 = \frac{-\frac{\tilde{D}}{4}\left(\alpha_p\alpha_r\lambda_q\lambda_s + \alpha_p^2\lambda_s^2\right)}{\left[\left(\alpha_p - \alpha_r\right)^2 + 4\left(\lambda_q + \lambda_s\right)^2\right]^2};$$

$$\chi_4 = \frac{-\frac{\tilde{D}}{4}\left(\alpha_p\alpha_r\lambda_q\lambda_s - \alpha_p^2\lambda_s^2\right)}{\left[\left(\alpha_p + \alpha_r\right)^2 + 4\left(\lambda_q - \lambda_s\right)^2\right]^2};\ \chi_5 = \frac{\frac{\tilde{D}}{2}\alpha_p^2\lambda_s^2}{\left[\left(\alpha_p - \alpha_r\right)^2 + 4\lambda_s^2\right]^2};\ \chi_6 = \frac{-\frac{\tilde{D}}{2}\alpha_p^2\lambda_s^2}{\left[\left(\alpha_p + \alpha_r\right)^2 + 4\lambda_s^2\right]^2}$$

Appendix E: The coefficients in Eq. (32) for CCCC-SB boundary condition

$$\chi_1 = \frac{\frac{\tilde{D}}{16}\left(\alpha_p\alpha_r\lambda_q\lambda_s - \alpha_p^2\lambda_s^2\right)}{\left[\left(\alpha_p - \alpha_r\right)^2 + \left(\lambda_q - \lambda_s\right)^2\right]^2};\ (\text{with } p = r \text{ và } q = s:\ \chi_1 = 0);$$

$$\chi_2 = \frac{\frac{\tilde{D}}{16}\left(\alpha_p\alpha_r\lambda_q\lambda_s - \alpha_p^2\lambda_s^2\right)}{\left[\left(\alpha_p + \alpha_r\right)^2 + \left(\lambda_q + \lambda_s\right)^2\right]^2};\ \chi_3 = \frac{-\frac{\tilde{D}}{16}\left(\alpha_p\alpha_r\lambda_q\lambda_s + \alpha_p^2\lambda_s^2\right)}{\left[\left(\alpha_p - \alpha_r\right)^2 + \left(\lambda_q + \lambda_s\right)^2\right]^2};$$

$$\chi_4 = \frac{-\frac{\tilde{D}}{16}\left(\alpha_p\alpha_r\lambda_q\lambda_s + \alpha_p^2\lambda_s^2\right)}{\left[\left(\alpha_p + \alpha_r\right)^2 + \left(\lambda_q - \lambda_s\right)^2\right]^2};\ \chi_5 = \frac{-\frac{\tilde{D}}{4}\alpha_p^2\lambda_s^2}{\left(\alpha_p^2 + \lambda_s^2\right)^2};\ \chi_6 = \frac{\frac{\tilde{D}}{8}\alpha_p^2\lambda_s^2}{\left[\alpha_p^2 + \left(\lambda_q - \lambda_s\right)^2\right]^2};$$

$$\chi_7 = \frac{\frac{\tilde{D}}{8}\alpha_p^2\lambda_s^2}{\left[\alpha_p^2 + \left(\lambda_q + \lambda_s\right)^2\right]^2};\ \chi_8 = \frac{\frac{\tilde{D}}{8}\alpha_p^2\lambda_s^2}{\left[\left(\alpha_p - \alpha_r\right)^2 + \lambda_s^2\right]^2};\ \chi_9 = \frac{\frac{\tilde{D}}{8}\alpha_p^2\lambda_s^2}{\left[\left(\alpha_p + \alpha_r\right)^2 + \lambda_s^2\right]^2};$$

Appendix F: The coefficients $\zeta^{(1)}_{pqrs}$, $\zeta^{(2)}_{pqrs}$ in Eq. (33)

Boundary condition SSSS-SB:

$$\zeta^{(1)}_{pqrs}=\frac{1}{ab}\int_0^b\int_0^a\left\{\begin{array}{l}\chi_1\dfrac{(q-s)^2\pi^2}{b^2}\cos\dfrac{(p-r)\pi x}{a}\cos\dfrac{(q-s)\pi y}{b}\\+\chi_2\dfrac{(q+s)^2\pi^2}{b^2}\cos\dfrac{(p+r)\pi x}{a}\cos\dfrac{(q+s)\pi y}{b}\\+\chi_3\dfrac{(q+s)^2\pi^2}{b^2}\cos\dfrac{(p-r)\pi x}{a}\cos\dfrac{(q+s)\pi y}{b}\\+\chi_4\dfrac{(q-s)^2\pi^2}{b^2}\cos\dfrac{(p+r)\pi x}{a}\cos\dfrac{(q-s)\pi y}{b}\\+\dfrac{\tilde{A}_{11}}{2}\dfrac{p\pi}{a}\dfrac{r\pi}{a}\cos\dfrac{p\pi x}{a}\cos\dfrac{r\pi x}{a}\sin\dfrac{q\pi y}{b}\sin\dfrac{s\pi y}{b}\\+\dfrac{\tilde{A}_{12}}{2}\dfrac{q\pi}{b}\dfrac{s\pi}{b}\sin\dfrac{p\pi x}{a}\sin\dfrac{r\pi x}{a}\cos\dfrac{q\pi y}{b}\cos\dfrac{s\pi y}{b}\end{array}\right\}\mathrm{d}x\mathrm{d}y;$$

$$\zeta^{(2)}_{pqrs}=\frac{1}{ab}\int_0^b\int_0^a\left\{\begin{array}{l}\chi_1\dfrac{(p-r)^2\pi^2}{a^2}\cos\dfrac{(p-r)\pi x}{a}\cos\dfrac{(q-s)\pi y}{b}\\+\chi_2\dfrac{(p+r)^2\pi^2}{a^2}\cos\dfrac{(p+r)\pi x}{a}\cos\dfrac{(q+s)\pi y}{b}\\+\chi_3\dfrac{(p-r)^2\pi^2}{a^2}\cos\dfrac{(p-r)\pi x}{a}\cos\dfrac{(q+s)\pi y}{b}\\+\chi_4\dfrac{(p+r)^2\pi^2}{a^2}\cos\dfrac{(p+r)\pi x}{a}\cos\dfrac{(q-s)\pi y}{b}\\+\dfrac{\tilde{A}_{12}}{2}\dfrac{p\pi}{a}\dfrac{r\pi}{a}\cos\dfrac{p\pi x}{a}\cos\dfrac{r\pi x}{a}\sin\dfrac{q\pi y}{b}\sin\dfrac{s\pi y}{b}\\+\dfrac{\tilde{A}_{11}}{2}\dfrac{q\pi}{b}\dfrac{s\pi}{b}\sin\dfrac{p\pi x}{a}\sin\dfrac{r\pi x}{a}\cos\dfrac{q\pi y}{b}\cos\dfrac{s\pi y}{b}\end{array}\right\}\mathrm{d}x\mathrm{d}y;$$

Boundary condition SCSC-SB:

$$\zeta_{pqrs}^{(1)}=\frac{1}{ab}\int_0^b\int_0^a\left\{\begin{array}{l}\chi_1\dfrac{4(q-s)^2\pi^2}{b^2}\cos\dfrac{(p-r)\pi x}{a}\cos\dfrac{2(q-s)\pi y}{b}\\+\chi_2\dfrac{4(q+s)^2\pi^2}{b^2}\cos\dfrac{(p+r)\pi x}{a}\cos\dfrac{2(q+s)\pi y}{b}\\+\chi_3\dfrac{4(q+s)^2\pi^2}{b^2}\cos\dfrac{(p-r)\pi x}{a}\cos\dfrac{2(q+s)\pi y}{b}\\+\chi_4\dfrac{4(q-s)^2\pi^2}{b^2}\cos\dfrac{(p+r)\pi x}{a}\cos\dfrac{2(q-s)\pi y}{b}\\+\chi_5\dfrac{4s^2\pi^2}{b^2}\cos\dfrac{(p-r)\pi x}{a}\cos\dfrac{2s\pi y}{b}\\+\chi_6\dfrac{4s^2\pi^2}{b^2}\cos\dfrac{(p+r)\pi x}{a}\cos\dfrac{2s\pi y}{b}\\+\dfrac{\tilde{A}_{11}}{2}\dfrac{p\pi}{a}\dfrac{r\pi}{a}\cos\dfrac{p\pi x}{a}\cos\dfrac{r\pi x}{a}\sin^2\dfrac{q\pi y}{b}\sin^2\dfrac{s\pi y}{b}\\+\dfrac{\tilde{A}_{12}}{2}\dfrac{q\pi}{b}\dfrac{s\pi}{b}\sin\dfrac{p\pi x}{a}\sin\dfrac{r\pi x}{a}\sin\dfrac{2q\pi y}{b}\sin\dfrac{2s\pi y}{b}\end{array}\right\}\mathrm{d}x\mathrm{d}y;$$

$$\zeta_{pqrs}^{(2)}=\frac{1}{ab}\int_0^b\int_0^a\left\{\begin{array}{l}\chi_1\dfrac{(p-r)^2\pi^2}{a^2}\cos\dfrac{(p-r)\pi x}{a}\cos\dfrac{2(q-s)\pi y}{b}\\+\chi_2\dfrac{(p+r)^2\pi^2}{a^2}\cos\dfrac{(p+r)\pi x}{a}\cos\dfrac{2(q+s)\pi y}{b}\\+\chi_3\dfrac{(p-r)^2\pi^2}{a^2}\cos\dfrac{(p-r)\pi x}{a}\cos\dfrac{2(q+s)\pi y}{b}\\+\chi_4\dfrac{(p+r)^2\pi^2}{a^2}\cos\dfrac{(p+r)\pi x}{a}\cos\dfrac{2(q-s)\pi y}{b}\\+\chi_5\dfrac{(p-r)^2\pi^2}{a^2}\cos\dfrac{(p-r)\pi x}{a}\cos\dfrac{2s\pi y}{b}\\+\chi_6\dfrac{(p+r)^2\pi^2}{a^2}\cos\dfrac{(p+r)\pi x}{a}\cos\dfrac{2s\pi y}{b}\\+\dfrac{\tilde{A}_{12}}{2}\dfrac{p\pi}{a}\dfrac{r\pi}{a}\cos\dfrac{p\pi x}{a}\cos\dfrac{r\pi x}{a}\sin^2\dfrac{q\pi y}{b}\sin^2\dfrac{s\pi y}{b}\\+\dfrac{\tilde{A}_{11}}{2}\dfrac{q\pi}{b}\dfrac{s\pi}{b}\sin\dfrac{p\pi x}{a}\sin\dfrac{r\pi x}{a}\sin\dfrac{2q\pi y}{b}\sin\dfrac{2s\pi y}{b}\end{array}\right\}\mathrm{d}x\mathrm{d}y;$$

Boundary condition CCCC-SB:

$$\zeta_{pqrs}^{(1)}=\frac{1}{ab}\int_0^b\int_0^a\left\{\begin{array}{l}\chi_1\dfrac{4(q-s)^2\pi^2}{b^2}\cos\dfrac{2(p-r)\pi x}{a}\cos\dfrac{2(q-s)\pi y}{b}\\+\chi_2\dfrac{4(q+s)^2\pi^2}{b^2}\cos\dfrac{2(p+r)\pi x}{a}\cos\dfrac{2(q+s)\pi y}{b}\\+\chi_3\dfrac{4(q+s)^2\pi^2}{b^2}\cos\dfrac{2(p-r)\pi x}{a}\cos\dfrac{2(q+s)\pi y}{b}\\+\chi_4\dfrac{4(q-s)^2\pi^2}{b^2}\cos\dfrac{2(p+r)\pi x}{a}\cos\dfrac{2(q-s)\pi y}{b}\\+\chi_5\dfrac{4s^2\pi^2}{b^2}\cos\dfrac{2p\pi x}{a}\cos\dfrac{2s\pi y}{b}\\+\chi_6\dfrac{4(q-s)^2\pi^2}{b^2}\cos\dfrac{2p\pi x}{a}\cos\dfrac{2(q-s)\pi y}{b}\\+\chi_7\dfrac{4(q+s)^2\pi^2}{b^2}\cos\dfrac{2p\pi x}{a}\cos\dfrac{2(q+s)\pi y}{b}\\+\chi_8\dfrac{4s^2\pi^2}{b^2}\cos\dfrac{2(p-r)\pi x}{a}\cos\dfrac{2s\pi y}{b}\\+\chi_9\dfrac{4s^2\pi^2}{b^2}\cos\dfrac{2(p+r)\pi x}{a}\cos\dfrac{2s\pi y}{b}\\+\dfrac{\tilde{A}_{11}}{2}\dfrac{p\pi}{a}\dfrac{r\pi}{a}\sin\dfrac{2p\pi x}{a}\sin\dfrac{2r\pi x}{a}\sin^2\dfrac{q\pi y}{b}\sin^2\dfrac{s\pi y}{b}\\+\dfrac{\tilde{A}_{12}}{2}\dfrac{q\pi}{b}\dfrac{s\pi}{b}\sin^2\dfrac{p\pi x}{a}\sin^2\dfrac{r\pi x}{a}\sin\dfrac{2q\pi y}{b}\sin\dfrac{2s\pi y}{b}\end{array}\right\}\mathrm{d}x\mathrm{d}y;$$

$$\zeta_{pqrs}^{(2)}=\frac{1}{ab}\int_0^b\int_0^a\left\{\begin{array}{l}\chi_1\dfrac{4(p-r)^2\pi^2}{a^2}\cos\dfrac{2(p-r)\pi x}{a}\cos\dfrac{2(q-s)\pi y}{b}\\+\chi_2\dfrac{4(p+r)^2\pi^2}{a^2}\cos\dfrac{2(p+r)\pi x}{a}\cos\dfrac{2(q+s)\pi y}{b}\\+\chi_3\dfrac{4(p-r)^2\pi^2}{a^2}\cos\dfrac{2(p-r)\pi x}{a}\cos\dfrac{2(q+s)\pi y}{b}\\+\chi_4\dfrac{4(p+r)^2\pi^2}{a^2}\cos\dfrac{2(p+r)\pi x}{a}\cos\dfrac{2(q-s)\pi y}{b}\\+\chi_5\dfrac{4p^2\pi^2}{a^2}\cos\dfrac{2p\pi x}{a}\cos\dfrac{2s\pi y}{b}\\+\chi_6\dfrac{4p^2\pi^2}{a^2}\cos\dfrac{2p\pi x}{a}\cos\dfrac{2(q-s)\pi y}{b}\\+\chi_7\dfrac{4p^2\pi^2}{a^2}\cos\dfrac{2p\pi x}{a}\cos\dfrac{2(q+s)\pi y}{b}\\+\chi_8\dfrac{4(p-r)^2\pi^2}{a^2}\cos\dfrac{2(p-r)\pi x}{a}\cos\dfrac{2s\pi y}{b}\\+\chi_9\dfrac{4(p+r)^2\pi^2}{a^2}\cos\dfrac{2(p+r)\pi x}{a}\cos\dfrac{2s\pi y}{b}\\+\dfrac{\tilde{A}_{12}}{2}\dfrac{p\pi}{a}\dfrac{r\pi}{a}\sin\dfrac{2p\pi x}{a}\sin\dfrac{2r\pi x}{a}\sin^2\dfrac{q\pi y}{b}\sin^2\dfrac{s\pi y}{b}\\+\dfrac{\tilde{A}_{11}}{2}\dfrac{q\pi}{b}\dfrac{s\pi}{b}\sin^2\dfrac{p\pi x}{a}\sin^2\dfrac{r\pi x}{a}\sin\dfrac{2q\pi y}{b}\sin\dfrac{2s\pi y}{b}\end{array}\right\}\mathrm{d}x\mathrm{d}y;$$

Appendix G: The function $g^{(3)}_{mnpqrs}$ in Eq. (34)

Boundary condition SSSS-SB:

$$\tilde{g}^{(3)}_{mnpqrs} = \tilde{g}^{(3a)}_{mnpqrs} + \tilde{g}^{(3b)}_{mnpqrs} + \tilde{g}^{(3c)}_{mnpqrs};$$

$$\begin{aligned}
\tilde{g}^{(3a)}_{mnpqrs} =& \tilde{H}_{1\mathrm{a}} \cos\frac{(p-r)\pi x}{a} \sin\frac{m\pi x}{a} \cos\frac{(q-s)\pi y}{b} \sin\frac{n\pi y}{b} \\
&+ \tilde{H}_{2\mathrm{a}} \cos\frac{(p+r)\pi x}{a} \sin\frac{m\pi x}{a} \cos\frac{(q+s)\pi y}{b} \sin\frac{n\pi y}{b} \\
&+ \tilde{H}_{3\mathrm{a}} \cos\frac{(p-r)\pi x}{a} \sin\frac{m\pi x}{a} \cos\frac{(q+s)\pi y}{b} \sin\frac{n\pi y}{b} \\
&+ \tilde{H}_{4\mathrm{a}} \cos\frac{(p+r)\pi x}{a} \sin\frac{m\pi x}{a} \cos\frac{(q-s)\pi y}{b} \sin\frac{n\pi y}{b}; \\
\tilde{g}^{(3b)}_{mnpqrs} =& -2\tilde{H}_{1b} \sin\frac{(p-r)\pi x}{a} \cos\frac{m\pi x}{a} \sin\frac{(q-s)\pi y}{b} \cos\frac{n\pi y}{b} \\
&- 2\tilde{H}_{2b} \sin\frac{(p+r)\pi x}{a} \cos\frac{m\pi x}{a} \sin\frac{(q+s)\pi y}{b} \cos\frac{n\pi y}{b} \\
&- 2\tilde{H}_{3b} \sin\frac{(p-r)\pi x}{a} \cos\frac{m\pi x}{a} \sin\frac{(q+s)\pi y}{b} \cos\frac{n\pi y}{b} \\
&- 2\tilde{H}_{4b} \sin\frac{(p+r)\pi x}{a} \cos\frac{m\pi x}{a} \sin\frac{(q-s)\pi y}{b} \cos\frac{n\pi y}{b}; \\
\tilde{g}^{(3c)}_{mnpqrs} =& -\left(\zeta^{(1)}_{pqrs}\alpha_m^2 + \zeta^{(2)}_{pqrs}\lambda_n^2\right) \sin\frac{m\pi x}{a} \sin\frac{n\pi y}{b};
\end{aligned}$$

in which:

$$\begin{aligned}
\tilde{H}_{1\mathrm{a}} &= \chi_1\left[\left(\lambda_q - \lambda_s\right)^2\alpha_m^2 + \left(\alpha_p - \alpha_r\right)^2\lambda_n^2\right];\ \tilde{H}_{2\mathrm{a}} = \chi_2\left[\left(\lambda_q + \lambda_s\right)^2\alpha_m^2 + \left(\alpha_p + \alpha_r\right)^2\lambda_n^2\right]; \\
\tilde{H}_{3\mathrm{a}} &= \chi_3\left[\left(\lambda_q + \lambda_s\right)^2\alpha_m^2 + \left(\alpha_p - \alpha_r\right)^2\lambda_n^2\right];\ \tilde{H}_{4\mathrm{a}} = \chi_4\left[\left(\lambda_q - \lambda_s\right)^2\alpha_m^2 + \left(\alpha_p + \alpha_r\right)^2\lambda_n^2\right]; \\
\tilde{H}_{1b} &= \chi_1\left(\alpha_p - \alpha_r\right)\left(\lambda_q - \lambda_s\right)\alpha_m\lambda_n;\ \tilde{H}_{2b} = \chi_2\left(\alpha_p + \alpha_r\right)\left(\lambda_q + \lambda_s\right)\alpha_m\lambda_n; \\
\tilde{H}_{3b} &= \chi_3\left(\alpha_p - \alpha_r\right)\left(\lambda_q + \lambda_s\right)\alpha_m\lambda_n;\ \tilde{H}_{4b} = \chi_4\left(\alpha_p + \alpha_r\right)\left(\lambda_q - \lambda_s\right)\alpha_m\lambda_n;
\end{aligned}$$

Boundary condition CCCC-SB:

$$\tilde{g}^{(3)}_{mnpqrs} = \tilde{g}^{(3a)}_{mnpqrs} + \tilde{g}^{(3b)}_{mnpqrs} + \tilde{g}^{(3c)}_{mnpqrs} + \tilde{g}^{(3d)}_{mnpqrs};$$

$$\begin{aligned}
\tilde{g}^{(3a)}_{mnpqrs} =& -8\chi_1\frac{m^2\pi^2}{a^2}\frac{(q-s)^2\pi^2}{b^2} \cos\frac{2(p-r)\pi x}{a} \cos\frac{2(q-s)\pi y}{b} \cos\frac{2m\pi x}{a} \sin^2\frac{n\pi y}{b} \\
&- 8\chi_2\frac{m^2\pi^2}{a^2}\frac{(q+s)^2\pi^2}{b^2} \cos\frac{2(p+r)\pi x}{a} \cos\frac{2(q+s)\pi y}{b} \cos\frac{2m\pi x}{a} \sin^2\frac{n\pi y}{b} \\
&- 8\chi_3\frac{m^2\pi^2}{a^2}\frac{(q+s)^2\pi^2}{b^2} \cos\frac{2(p-r)\pi x}{a} \cos\frac{2(q+s)\pi y}{b} \cos\frac{2m\pi x}{a} \sin^2\frac{n\pi y}{b} \\
&- 8\chi_4\frac{m^2\pi^2}{a^2}\frac{(q-s)^2\pi^2}{b^2} \cos\frac{2(p+r)\pi x}{a} \cos\frac{2(q-s)\pi y}{b} \cos\frac{2m\pi x}{a} \sin^2\frac{n\pi y}{b} \\
&- 8\chi_5\frac{m^2\pi^2}{a^2}\frac{s^2\pi^2}{b^2} \cos\frac{2p\pi x}{a} \cos\frac{2s\pi y}{b} \cos\frac{2m\pi x}{a} \sin^2\frac{n\pi y}{b} \\
&- 8\chi_6\frac{m^2\pi^2}{a^2}\frac{(q-s)^2\pi^2}{b^2} \cos\frac{2p\pi x}{a} \cos\frac{2(q-s)\pi y}{b} \cos\frac{2m\pi x}{a} \sin^2\frac{n\pi y}{b} \\
&- 8\chi_7\frac{m^2\pi^2}{a^2}\frac{(q+s)^2\pi^2}{b^2} \cos\frac{2p\pi x}{a} \cos\frac{2(q+s)\pi y}{b} \cos\frac{2m\pi x}{a} \sin^2\frac{n\pi y}{b}
\end{aligned}$$

$$
\begin{aligned}
&-8\chi_8\frac{m^2\pi^2}{a^2}\frac{s^2\pi^2}{b^2}\cos\frac{2(p-r)\pi x}{a}\cos\frac{2s\pi y}{b}\cos\frac{2m\pi x}{a}\sin^2\frac{n\pi y}{b}\\
&-8\chi_9\frac{m^2\pi^2}{a^2}\frac{s^2\pi^2}{b^2}\cos\frac{2(p+r)\pi x}{a}\cos\frac{2s\pi y}{b}\cos\frac{2m\pi x}{a}\sin^2\frac{n\pi y}{b};
\end{aligned}
$$

$$
\begin{aligned}
\tilde{g}^{(3b)}_{mnpqrs} =&-8\chi_1\frac{m\pi}{a}\frac{n\pi}{b}\frac{(p-r)\pi}{a}\frac{(q-s)\pi}{b}\cos\frac{2(p-r)\pi x}{a}\cos\frac{2(q-s)\pi y}{b}\sin\frac{2m\pi x}{a}\sin\frac{2n\pi y}{b}\\
&-8\chi_2\frac{m\pi}{a}\frac{n\pi}{b}\frac{(p+r)\pi}{a}\frac{(q+s)\pi}{b}\cos\frac{2(p+r)\pi x}{a}\cos\frac{2(q+s)\pi y}{b}\sin\frac{2m\pi x}{a}\sin\frac{2n\pi y}{b}\\
&-8\chi_3\frac{m\pi}{a}\frac{n\pi}{b}\frac{(p-r)\pi}{a}\frac{(q+s)\pi}{b}\cos\frac{2(p-r)\pi x}{a}\cos\frac{2(q+s)\pi y}{b}\sin\frac{2m\pi x}{a}\sin\frac{2n\pi y}{b}\\
&-8\chi_4\frac{m\pi}{a}\frac{n\pi}{b}\frac{(p+r)\pi}{a}\frac{(q-s)\pi}{b}\cos\frac{2(p+r)\pi x}{a}\cos\frac{2(q-s)\pi y}{b}\sin\frac{2m\pi x}{a}\sin\frac{2n\pi y}{b}\\
&-8\chi_5\frac{m\pi}{a}\frac{n\pi}{b}\frac{p\pi}{a}\frac{s\pi}{b}\cos\frac{2p\pi x}{a}\cos\frac{2s\pi y}{b}\sin\frac{2m\pi x}{a}\sin\frac{2n\pi y}{b}\\
&-8\chi_6\frac{m\pi}{a}\frac{n\pi}{b}\frac{p\pi}{a}\frac{(q-s)\pi}{b}\cos\frac{2p\pi x}{a}\cos\frac{2(q-s)\pi y}{b}\sin\frac{2m\pi x}{a}\sin\frac{2n\pi y}{b}\\
&-8\chi_7\frac{m\pi}{a}\frac{n\pi}{b}\frac{p\pi}{a}\frac{(q+s)\pi}{b}\cos\frac{2p\pi x}{a}\cos\frac{2(q+s)\pi y}{b}\sin\frac{2m\pi x}{a}\sin\frac{2n\pi y}{b}\\
&-8\chi_8\frac{m\pi}{a}\frac{n\pi}{b}\frac{(p-r)\pi}{a}\frac{s\pi}{b}\cos\frac{2(p-r)\pi x}{a}\cos\frac{2s\pi y}{b}\sin\frac{2m\pi x}{a}\sin\frac{2n\pi y}{b}\\
&-8\chi_9\frac{m\pi}{a}\frac{n\pi}{b}\frac{(p+r)\pi}{a}\frac{s\pi}{b}\cos\frac{2(p+r)\pi x}{a}\cos\frac{2s\pi y}{b}\sin\frac{2m\pi x}{a}\sin\frac{2n\pi y}{b};
\end{aligned}
$$

$$
\begin{aligned}
\tilde{g}^{(3c)}_{mnpqrs} =&-8\chi_1\frac{n^2\pi^2}{b^2}\frac{(p-r)^2\pi^2}{a^2}\cos\frac{2(p-r)\pi x}{a}\cos\frac{2(q-s)\pi y}{b}\sin^2\frac{m\pi x}{a}\cos\frac{2n\pi y}{b}\\
&-8\chi_2\frac{n^2\pi^2}{b^2}\frac{(p+r)^2\pi^2}{a^2}\cos\frac{2(p+r)\pi x}{a}\cos\frac{2(q+s)\pi y}{b}\sin^2\frac{m\pi x}{a}\cos\frac{2n\pi y}{b}\\
&-8\chi_3\frac{n^2\pi^2}{b^2}\frac{(p-r)^2\pi^2}{a^2}\cos\frac{2(p-r)\pi x}{a}\cos\frac{2(q+s)\pi y}{b}\sin^2\frac{m\pi x}{a}\cos\frac{2n\pi y}{b}\\
&-8\chi_4\frac{n^2\pi^2}{b^2}\frac{(p+r)^2\pi^2}{a^2}\cos\frac{2(p+r)\pi x}{a}\cos\frac{2(q-s)\pi y}{b}\sin^2\frac{m\pi x}{a}\cos\frac{2n\pi y}{b}\\
&-8\chi_5\frac{n^2\pi^2}{b^2}\frac{p^2\pi^2}{a^2}\cos\frac{2p\pi x}{a}\cos\frac{2s\pi y}{b}\sin^2\frac{m\pi x}{a}\cos\frac{2n\pi y}{b}\\
&-8\chi_6\frac{n^2\pi^2}{b^2}\frac{p^2\pi^2}{a^2}\cos\frac{2p\pi x}{a}\cos\frac{2(q-s)\pi y}{b}\sin^2\frac{m\pi x}{a}\cos\frac{2n\pi y}{b}\\
&-8\chi_7\frac{n^2\pi^2}{b^2}\frac{p^2\pi^2}{a^2}\cos\frac{2p\pi x}{a}\cos\frac{2(q+s)\pi y}{b}\sin^2\frac{m\pi x}{a}\cos\frac{2n\pi y}{b}\\
&-8\chi_8\frac{n^2\pi^2}{b^2}\frac{(p-r)^2\pi^2}{a^2}\cos\frac{2(p-r)\pi x}{a}\cos\frac{2s\pi y}{b}\sin^2\frac{m\pi x}{a}\cos\frac{2n\pi y}{b}\\
&-8\chi_9\frac{n^2\pi^2}{b^2}\frac{(p+r)^2\pi^2}{a^2}\cos\frac{2(p+r)\pi x}{a}\cos\frac{2s\pi y}{b}\sin^2\frac{m\pi x}{a}\cos\frac{2n\pi y}{b};
\end{aligned}
$$

$$
\tilde{g}^{(3d)}_{mnpqrs} = 2\zeta^{(1)}_{pqrs}\alpha_m^2\cos\frac{2m\pi x}{a}\sin^2\frac{n\pi y}{b}+2\zeta^{(2)}_{pqrs}\lambda_n^2\sin^2\frac{m\pi x}{a}\cos\frac{2n\pi y}{b};
$$

Boundary condition SCSC-SB:

$$
\tilde{g}^{(3)}_{mnpqrs} = \tilde{g}^{(3a)}_{mnpqrs}+\tilde{g}^{(3b)}_{mnpqrs}+\tilde{g}^{(3c)}_{mnpqrs}+\tilde{g}^{(3d)}_{mnpqrs};
$$

$$
\tilde{g}^{(3a)}_{mnpqrs} =\chi_1\frac{4(q-s)^2\pi^2}{b^2}\frac{m^2\pi^2}{a^2}\cos\frac{(p-r)\pi x}{a}\cos\frac{2(q-s)\pi y}{b}\sin\frac{m\pi x}{a}\sin^2\frac{n\pi y}{b}
$$

$$
\begin{aligned}
&+\chi_2\frac{4(q+s)^2\pi^2}{b^2}\frac{m^2\pi^2}{a^2}\cos\frac{(p+r)\pi x}{a}\cos\frac{2(q+s)\pi y}{b}\sin\frac{m\pi x}{a}\sin^2\frac{n\pi y}{b}\\
&+\chi_3\frac{4(q+s)^2\pi^2}{b^2}\frac{m^2\pi^2}{a^2}\cos\frac{(p-r)\pi x}{a}\cos\frac{2(q+s)\pi y}{b}\sin\frac{m\pi x}{a}\sin^2\frac{n\pi y}{b}\\
&+\chi_4\frac{4(q-s)^2\pi^2}{b^2}\frac{m^2\pi^2}{a^2}\cos\frac{(p+r)\pi x}{a}\cos\frac{2(q-s)\pi y}{b}\sin\frac{m\pi x}{a}\sin^2\frac{n\pi y}{b}\\
&+\chi_5\frac{4s^2\pi^2}{b^2}\frac{m^2\pi^2}{a^2}\cos\frac{(p-r)\pi x}{a}\cos\frac{2s\pi y}{b}\sin\frac{m\pi x}{a}\sin^2\frac{n\pi y}{b}\\
&+\chi_6\frac{4s^2\pi^2}{b^2}\frac{m^2\pi^2}{a^2}\cos\frac{(p+r)\pi x}{a}\cos\frac{2s\pi y}{b}\sin\frac{m\pi x}{a}\sin^2\frac{n\pi y}{b};
\end{aligned}
$$

$$
\begin{aligned}
\tilde{g}^{(3b)}_{mnpqrs} =&-\chi_1\frac{4(p-r)\pi}{a}\frac{(q-s)\pi}{b}\frac{m\pi}{a}\frac{n\pi}{b}\cos\frac{(p-r)\pi x}{a}\cos\frac{2(q-s)\pi y}{b}\cos\frac{m\pi x}{a}\sin\frac{2n\pi y}{b}\\
&-\chi_2\frac{4(p+r)\pi}{a}\frac{(q+s)\pi}{b}\frac{m\pi}{a}\frac{n\pi}{b}\cos\frac{(p+r)\pi x}{a}\cos\frac{2(q+s)\pi y}{b}\cos\frac{m\pi x}{a}\sin\frac{2n\pi y}{b}\\
&-\chi_3\frac{4(p-r)\pi}{a}\frac{(q+s)\pi}{b}\frac{m\pi}{a}\frac{n\pi}{b}\cos\frac{(p-r)\pi x}{a}\cos\frac{2(q+s)\pi y}{b}\cos\frac{m\pi x}{a}\sin\frac{2n\pi y}{b}\\
&-\chi_4\frac{4(p+r)\pi}{a}\frac{(q-s)\pi}{b}\frac{m\pi}{a}\frac{n\pi}{b}\cos\frac{(p+r)\pi x}{a}\cos\frac{2(q-s)\pi y}{b}\cos\frac{m\pi x}{a}\sin\frac{2n\pi y}{b}\\
&-\chi_5\frac{4(p-r)\pi}{a}\frac{s\pi}{b}\frac{m\pi}{a}\frac{n\pi}{b}\cos\frac{(p-r)\pi x}{a}\cos\frac{2s\pi y}{b}\cos\frac{m\pi x}{a}\sin\frac{2n\pi y}{b}\\
&-\chi_6\frac{4(p+r)\pi}{a}\frac{s\pi}{b}\frac{m\pi}{a}\frac{n\pi}{b}\cos\frac{(p+r)\pi x}{a}\cos\frac{2s\pi y}{b}\cos\frac{m\pi x}{a}\sin\frac{2n\pi y}{b};
\end{aligned}
$$

$$
\begin{aligned}
\tilde{g}^{(3c)}_{mnpqrs} =&-2\chi_1\frac{(p-r)^2\pi^2}{a^2}\frac{n^2\pi^2}{b^2}\cos\frac{(p-r)\pi x}{a}\cos\frac{2(q-s)\pi y}{b}\sin\frac{m\pi x}{a}\cos\frac{2n\pi y}{b}\\
&-2\chi_2\frac{(p+r)^2\pi^2}{a^2}\frac{n^2\pi^2}{b^2}\cos\frac{(p+r)\pi x}{a}\cos\frac{2(q+s)\pi y}{b}\sin\frac{m\pi x}{a}\cos\frac{2n\pi y}{b}\\
&-2\chi_3\frac{(p-r)^2\pi^2}{a^2}\frac{n^2\pi^2}{b^2}\cos\frac{(p-r)\pi x}{a}\cos\frac{2(q+s)\pi y}{b}\sin\frac{m\pi x}{a}\cos\frac{2n\pi y}{b}\\
&-2\chi_4\frac{(p+r)^2\pi^2}{a^2}\frac{n^2\pi^2}{b^2}\cos\frac{(p+r)\pi x}{a}\cos\frac{2(q-s)\pi y}{b}\sin\frac{m\pi x}{a}\cos\frac{2n\pi y}{b}\\
&-2\chi_5\frac{(p-r)^2\pi^2}{a^2}\frac{n^2\pi^2}{b^2}\cos\frac{(p-r)\pi x}{a}\cos\frac{2s\pi y}{b}\sin\frac{m\pi x}{a}\cos\frac{2n\pi y}{b}\\
&-2\chi_6\frac{(p+r)^2\pi^2}{a^2}\frac{n^2\pi^2}{b^2}\cos\frac{(p+r)\pi x}{a}\cos\frac{2s\pi y}{b}\sin\frac{m\pi x}{a}\cos\frac{2n\pi y}{b};
\end{aligned}
$$

$$
\tilde{g}^{(3d)}_{mnpqrs} = -\zeta^{(1)}_{pqrs}\alpha_m^2\sin\frac{m\pi x}{a}\sin^2\frac{n\pi y}{b}+2\zeta^{(2)}_{pqrs}\lambda_n^2\sin\frac{m\pi x}{a}\cos\frac{2n\pi y}{b}.
$$

References

1. Smith, B., et al.: Steel foam for structures: A review of applications, manufacturing and material properties. J. Constr. Steel Res. **71**, 1–10 (2012)
2. Ashby, M.F., et al.: Metal Foams: A Design Guide. Elsevier, Amsterdam (2000)
3. Banhart, J.: Manufacture, characterisation and application of cellular metals and metal foams. Prog. Mater Sci. **46**(6), 559–632 (2001)
4. Magnucki, K., Malinowski, M., Kasprzak, J.: Bending and buckling of a rectangular porous plate. Steel Compos. Struct. **6**(4), 319–333 (2006)
5. Jabbari, M., et al.: Buckling analysis of a functionally graded thin circular plate made of saturated porous materials. J. Eng. Mech. **140**(2), 287–295 (2014)
6. Chen, D., Yang, J., Kitipornchai, S.: Elastic buckling and static bending of shear deformable functionally graded porous beam. Compos. Struct. **133**, 54–61 (2015)
7. Wang, Y., Wu, D.: Free vibration of functionally graded porous cylindrical shell using a sinusoidal shear deformation theory. Aerosp. Sci. Technol. **66**, 83–91 (2017)

8. Ebrahimi, F., Dabbagh, A., Rastgoo, A.: Vibration analysis of porous metal foam shells rested on an elastic substrate. J. Strain Anal. Eng. Des. **54**(3), 199–208 (2019)
9. Zine, A., et al.: Bending analysis of functionally graded porous plates via a refined shear deformation theory. Comput. Concr. **26**(1), 63–74 (2020)
10. Dang, X.-H., et al.: Free vibration characteristics of rotating functionally graded porous circular cylindrical shells with different boundary conditions. Iran. J. Sci. Technol. Trans. Mech. Eng. (2020). https://doi.org/10.1007/s40997-020-00413-1
11. Masjedi, P.K., Maheri, A., Weaver, P.M.: Large deflection of functionally graded porous beams based on a geometrically exact theory with a fully intrinsic formulation. Appl. Math. Model. **76**, 938–957 (2019)
12. Praveen, G., Reddy, J.: Nonlinear transient thermoelastic analysis of functionally graded ceramic-metal plates. Int. J. Solids Struct. **35**(33), 4457–4476 (1998)
13. Aliaga, J., Reddy, J.: Nonlinear thermoelastic analysis of functionally graded plates using the third-order shear deformation theory. Int. J. Comput. Eng. Sci. **5**(04), 753–779 (2004)
14. Zhao, X., Liew, K.M.: Geometrically nonlinear analysis of functionally graded plates using the element-free kp-Ritz method. Comput. Methods Appl. Mech. Eng. **198**(33), 2796–2811 (2009)
15. Barbosa, J., Ferreira, A.: Geometrically nonlinear analysis of functionally graded plates and shells. Mech. Adv. Mater. Struct. **17**(1), 40–48 (2009)
16. Behjat, B., Khoshravan, M.: Geometrically nonlinear static and free vibration analysis of functionally graded piezoelectric plates. Compos. Struct. **94**(3), 874–882 (2012)
17. Singh, J., Shukla, K.: Nonlinear flexural analysis of functionally graded plates under different loadings using RBF based meshless method. Eng. Anal. Bound. Elem. **36**(12), 1819–1827 (2012)
18. Zhu, P., Zhang, L., Liew, K.: Geometrically nonlinear thermomechanical analysis of moderately thick functionally graded plates using a local Petrov-Galerkin approach with moving Kriging interpolation. Compos. Struct. **107**, 298–314 (2014)
19. Yin, S., et al.: Geometrically nonlinear analysis of functionally graded plates using isogeometric analysis. Eng. Comput. (2015). https://doi.org/10.1108/EC-09-2013-0220
20. Heydari, M.M., et al.: Nonlinear bending analysis of functionally graded CNT-reinforced composite Mindlin polymeric temperature-dependent plate resting on orthotropic elastomeric medium using GDQM. Nonlinear Dyn. **79**(2), 1425–1441 (2015)
21. Phung-Van, P., et al.: Geometrically nonlinear analysis of functionally graded plates using a cell-based smoothed three-node plate element (CS-MIN3) based on the C0-HSDT. Comput. Methods Appl. Mech. Eng. **270**, 15–36 (2014)
22. Nourmohammadi, H., Behjat, B.: Geometrically nonlinear analysis of functionally graded piezoelectric plate using mesh-free RPIM. Eng. Anal. Bound. Elem. **99**, 131–141 (2019)
23. TonThat, H.L., Nguyen-Van, H., Chau-Dinh, T.: Nonlinear bending analysis of functionally graded plates using SQ4T elements based on twice interpolation strategy. J. Appl. Comput. Mech. **6**(1), 125–136 (2020)
24. Shen, H.-S.: Nonlinear bending response of functionally graded plates subjected to transverse loads and in thermal environments. Int. J. Mech. Sci. **44**(3), 561–584 (2002)
25. Yang, J., Shen, H.-S.: Nonlinear bending analysis of shear deformable functionally graded plates subjected to thermo-mechanical loads under various boundary conditions. Compos. B Eng. **34**(2), 103–115 (2003)
26. Shen, H.-S., Wang, Z.-X.: Nonlinear bending of FGM plates subjected to combined loading and resting on elastic foundations. Compos. Struct. **92**(10), 2517–2524 (2010)
27. Van Tung, H., Duc, N.D.: Nonlinear analysis of stability for functionally graded plates under mechanical and thermal loads. Compos. Struct. **92**(5), 1184–1191 (2010)
28. Thang, P.-T., Nguyen-Thoi, T., Lee, J.: Closed-form expression for nonlinear analysis of imperfect sigmoid-FGM plates with variable thickness resting on elastic medium. Compos. Struct. **143**, 143–150 (2016)
29. Duc, N.D., Bich, D.H., Cong, P.H.: Nonlinear thermal dynamic response of shear deformable FGM plates on elastic foundations. J. Therm. Stresses **39**(3), 278–297 (2016)
30. Woo, J., Meguid, S., Ong, L.: Nonlinear free vibration behavior of functionally graded plates. J. Sound Vib. **289**(3), 595–611 (2006)
31. Wu, T.-L., Shukla, K., Huang, J.H.: Post-buckling analysis of functionally graded rectangular plates. Compos. Struct. **81**(1), 1–10 (2007)
32. Alinia, M., Ghannadpour, S.: Nonlinear analysis of pressure loaded FGM plates. Compos. Struct. **88**(3), 354–359 (2009)
33. Woo, J., Meguid, S.: Nonlinear analysis of functionally graded plates and shallow shells. Int. J. Solids Struct. **38**(42–43), 7409–7421 (2001)
34. Khabbaz, R.S., Manshadi, B.D., Abedian, A.: Nonlinear analysis of FGM plates under pressure loads using the higher-order shear deformation theories. Compos. Struct. **89**(3), 333–344 (2009)
35. Benatta, M.A., et al.: Nonlinear bending analysis of functionally graded plates under pressure loads using a four variable refined plate theory. Int. J. Comput. Methods **11**(04), 1350062 (2014)
36. Dinh Duc, N., et al.: Nonlinear dynamic response of functionally graded porous plates on elastic foundation subjected to thermal and mechanical loads. J. Appl. Comput. Mech. **4**(4), 245–259 (2018)
37. Tu, T.M., et al.: Nonlinear buckling and post-buckling analysis of imperfect porous plates under mechanical loads. J. Sandw. Struct. Mater. (2018). https://doi.org/10.1177/1099636218789612
38. Cong, P.H., et al.: Nonlinear thermomechanical buckling and post-buckling response of porous FGM plates using Reddy's HSDT. Aerosp. Sci. Technol. **77**, 419–428 (2018)
39. Phung-Van, P., et al.: Isogeometric nonlinear transient analysis of porous FGM plates subjected to hygro-thermo-mechanical loads. Thin-Walled Struct. **148**, 106497 (2020)
40. Nguyen, N.V., et al.: Geometrically nonlinear polygonal finite element analysis of functionally graded porous plates. Adv. Eng. Softw. **126**, 110–126 (2018)
41. Ansari, R., et al.: Nonlinear bending analysis of arbitrary-shaped porous nanocomposite plates using a novel numerical approach. Int. J. Non-Linear Mech. **126**, 103556 (2020)

42. Nematollahi, M.S., et al.: Nonlinear vibration of functionally graded graphene nanoplatelets polymer nanocomposite sandwich beams. Appl. Sci. **10**(16), 5669 (2020)
43. Selvamani, R., et al.: Nonlinear magneto-thermo-elastic vibration of mass sensor armchair carbon nanotube resting on an elastic substrate. Curved Layer. Struct. **7**(1), 153–165 (2020)
44. Zhang, D.-G., Zhou, Y.-H.: A theoretical analysis of FGM thin plates based on physical neutral surface. Comput. Mater. Sci. **44**(2), 716–720 (2008)
45. Zhang, D.-G.: Modeling and analysis of FGM rectangular plates based on physical neutral surface and high order shear deformation theory. Int. J. Mech. Sci. **68**, 92–104 (2013)
46. Chen, D., Yang, J., Kitipornchai, S.: Free and forced vibrations of shear deformable functionally graded porous beams. Int. J. Mech. Sci. **108**, 14–22 (2016)
47. Barati, M.R., Zenkour, A.M.: Investigating post-buckling of geometrically imperfect metal foam nanobeams with symmetric and asymmetric porosity distributions. Compos. Struct. **182**, 91–98 (2017)
48. Magnucki, K., Stasiewicz, P.: Elastic buckling of a porous beam. J. Theor. Appl. Mech. **42**(4), 859–868 (2004)
49. Larbi, L.O., et al.: An efficient shear deformation beam theory based on neutral surface position for bending and free vibration of functionally graded beams#. Mech. Based Des. Struct. Mach. **41**(4), 421–433 (2013)
50. Reddy, J.N.: Theory and Analysis of Elastic Plates and Shells. CRC Press, Boca Raton (2006)
51. Reddy, J.N.: Energy Principles and Variational Methods in Applied Mechanics. Wiley, Hoboken (2017)
52. Sobhy, M.: Buckling and free vibration of exponentially graded sandwich plates resting on elastic foundations under various boundary conditions. Compos. Struct. **99**, 76–87 (2013)
53. Meziane, M.A.A., Abdelaziz, H.H., Tounsi, A.: An efficient and simple refined theory for buckling and free vibration of exponentially graded sandwich plates under various boundary conditions. J. Sandw. Struct. Mater. **16**(3), 293–318 (2014)
54. Brush, D.O., Almroth, B.O.: Buckling of Bars, Plates, and Shells, vol. 6. McGraw-Hill, New York (1975)
55. Librescu, L., Stein, M.: A geometrically nonlinear theory of transversely isotropic laminated composite plates and its use in the post-buckling analysis. Thin-Walled Struct. **11**(1–2), 177–201 (1991)
56. Shen, H.-S.: Thermal postbuckling behavior of shear deformable FGM plates with temperature-dependent properties. Int. J. Mech. Sci. **49**(4), 466–478 (2007)
57. Thai, H.-T., Choi, D.-H.: A refined plate theory for functionally graded plates resting on elastic foundation. Compos. Sci. Technol. **71**(16), 1850–1858 (2011)
58. Zenkour, A.M.: The refined sinusoidal theory for FGM plates on elastic foundations. Int. J. Mech. Sci. **51**(11–12), 869–880 (2009)
59. Lei, X.-Y., Huang, M.-K., Wang, X.: Geometrically nonlinear analysis of a Reissner type plate by the boundary element method. Comput. Struct. **37**(6), 911–916 (1990)
60. Azizian, Z., Dawe, D.: Geometrically nonlinear analysis of rectangular mindlin plates using the finite strip method. Comput. Struct. **21**(3), 423–436 (1985)
61. Talha, M., Singh, B.: Nonlinear mechanical bending of functionally graded material plates under transverse loads with various boundary conditions. Int. J. Model. Simul. Sci. Comput. **2**(02), 237–258 (2011)